

SPIN CURRENTS IN SEMICONDUCTOR NANOSTRUCTURES: A NONEQUILIBRIUM GREEN-FUNCTION APPROACH

Branislav K. Nikolić,¹ Liviu P. Zârbo,² and Satofumi Souma³

¹*Department of Physics and Astronomy, University of Delaware, Newark DE 19716, USA*

²*Department of Physics, Texas A&M University, College Station TX 77843-4242, USA*

³*Department of Electronics and Electrical Engineering, Kobe University, 1-1 Rokkodai, Nada, Kobe 657-8501, Japan*

Chapter 24, page 814–866 in Volume I of

The Oxford Handbook on Nanoscience and Technology: Frontiers and Advances
Eds. A. V. Narlikar and Y. Y. Fu (Oxford University Press, Oxford, 2010)

Contents

1	INTRODUCTION	3
2	WHAT IS PURE SPIN CURRENT?	5
3	HOW CAN PURE SPIN CURRENTS BE GENERATED AND DETECTED?	6
4	WHAT IS THE SPIN-HALL EFFECT?	6
5	WHAT IS THE MESOSCOPIC SPIN-HALL EFFECT?	8
6	SO COUPLINGS IN LOW-DIMENSIONAL SEMICONDUCTORS	10
6.1	Rashba coupling in bulk 2DEG	13
6.2	Rashba coupling in quantum wires	15
6.2.1	Energy dispersion of Rashba spin-split transverse propagating subbands	15
6.2.2	Spin precession in Rashba quantum wires	17
6.3	Discrete representation of effective SO Hamiltonians	18
6.3.1	Discretization of the Rashba SO Hamiltonian	19
6.3.2	Discretization of the extrinsic SO Hamiltonian	20
7	SPIN CURRENT OPERATOR, SPIN DENSITY, AND SPIN ACCUMULATION IN THE PRESENCE OF INTRINSIC SO COUPLINGS	21

arXiv:0907.4122v1 [cond-mat.mes-hall] 23 Jul 2009

8	NEGF APPROACH TO SPIN TRANSPORT IN MULTITERMINAL SO-COUPLED NANOSTRUCTURES	23
8.1	Landauer-Büttiker approach to total spin currents in multiterminal nanostructures	24
8.1.1	General expression for spin-Hall conductance	27
8.1.2	Symmetry properties of spin conductances	28
8.1.3	Example: Transverse total spin currents in mesoscopic and quantum-interference-driven SHE nanostructures	30
8.2	Landauer-Keldysh approach to local spin currents in multiterminal nanostructures	31
8.2.1	Bond charge current operator in SO-coupled systems	31
8.2.2	Nonequilibrium bond charge current in SO-coupled systems	32
8.2.3	Bond spin current operator in SO-coupled systems	34
8.2.4	Nonequilibrium bond spin currents in SO-coupled systems	34
8.3	Landauer-Keldysh approach to local spin densities	35
8.3.1	Local spin density and its continuity equation	35
8.4	Spin-resolved NEGFs for finite-size multiterminal devices	36
8.4.1	How to introduce dephasing into SHE nanostructures	38
8.5	Example: Local spin density and spin currents in mesoscopic SHE nanostructures	39
9	COMPUTATIONAL ALGORITHMS FOR REAL\otimesSPIN SPACE NEGFs IN MULTITERMINAL DEVICES	41
9.1	Numerical algorithms for computing self-energy matrices	41
9.2	Recursive Green function algorithm for total spin and charge currents in multiterminal nanostructures	43
9.3	Recursive Green function algorithm for local spin and charge densities	46
10	CONCLUDING REMARKS	47
	Acknowledgments	48
	References	48

1 INTRODUCTION

Over the past two decades, *spintronics* (Žutić et al., 2004) has emerged as one of the most vigorously pursued areas of condensed matter physics, materials science, and nanotechnology. A glimpse at the Oxford English Dictionary reveals the following attempt to define the field succinctly: “*spintronics is a branch of physics concerned with the storage and transfer of information by means of electron spins in addition to electron charge as in conventional electronics.*” The rise of spintronics was ignited by basic research on ferromagnet/normal-metal multilayers in late 1980s (Maekawa and Shinjo, 2002), as recognized by the Nobel Prize in Physics for 2007 being awarded to A. Fert and P. Grünberg for the discovery of giant magnetoresistance (GMR). The GMR phenomenon also exemplifies one of the fastest transfers of basic research results in condensed matter physics into applications where in less than ten years since its discovery it has revolutionized information storage technologies by enabling 100 times increase in hard disk storage capacity.

In recent years frontiers of spintronics have been reshaped through several intertwined lines of research: (*i*) ferromagnetic metal devices where the main theme is manipulation of magnetization via electric currents and vice versa (Ralph and Stiles, 2008); (*ii*) ferromagnetic semiconductors which, unlike metal ferromagnets, offer additional possibilities to manipulate their magnetic ordering (such as Curie temperature, coercive fields, and magnetic dopants), but are still below optimal operating temperature (Jungwirth et al., 2006); (*iii*) paramagnetic semiconductor spintronics (Awschalom and Flatté, 2007) largely focused on *all-electrical* manipulation of spins via spin-orbit (SO) coupling effects in solids (Fabian et al., 2007); and (*iv*) spins in semiconductors as building blocks of futuristic solid-state-based quantum computers (Hanson et al., 2007). Unlike early non-coherent spintronics phenomena (such as GMR), the major themes of the “second-generation” spintronics (Awschalom and Flatté, 2007) are moving toward the spin coherent realm where spin component persists in the direction transverse to external or effective internal magnetic fields. Recent experiments exploring such phenomena include: spin-transfer torque where spin current of large enough density injected into a ferromagnetic layer either switches its magnetization from one static configuration to another or generates a dynamical situation with steady-state precessing magnetization (Ralph and Stiles, 2008); spin pumping as the “inverse” effect of spin-transfer torque in which precessing magnetization of a ferromagnetic layer emits pure spin currents into adjacent normal metal layers in the absence of any bias voltage (Saitoh et al., 2006; Costache et al., 2006; Moriyama et al., 2008); transport of coherent spins (able to precess in the external magnetic fields) across $\sim 100 \mu\text{m}$ thick silicon wafers (Huang et al., 2007); and the direct and inverse spin-Hall effects (SHE) in bulk (Kato et al., 2004a) and low-dimensional (Wunderlich et al., 2005; Sih et al., 2005) semiconductors and metals (Valenzuela and Tinkham, 2006; Saitoh et al., 2006; Kimura et al., 2007) [SHE in both metals and semiconductors has been observed even at room temperature (Stern et al., 2006; Kimura et al., 2007)]. A closely related effort that permeates these subfields is the generation and detection of *pure spin currents* (Nagaosa, 2008) which do not transport any net charge, as illustrated in Fig. 1. Their harnessing is expected to offer both new functionality and greatly reduced power dissipation.¹

¹The Joule heat losses induced by the current flow set the most important limits (Keyes, 2005) for conventional electronics, as well as for hybrid electronic-spintronic or purely spintronic devices envisioned to perform

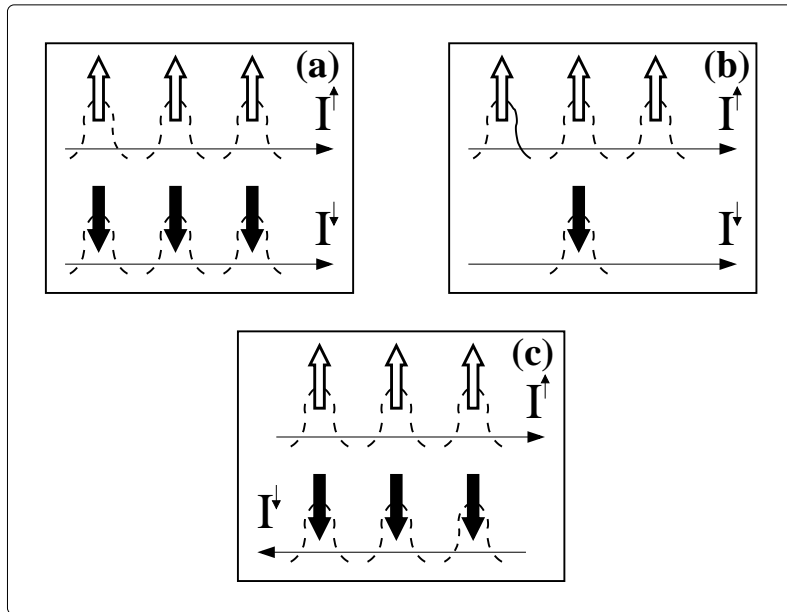


Figure 1: The classification of spin I^S and charge I currents in metal and semiconductor spintronic systems corresponding to spatial propagation of spin- \uparrow and spin- \downarrow electronic wave packets carrying spin-resolved currents I^\uparrow and I^\downarrow : (a) conventional charge current $I = I^\uparrow + I^\downarrow \neq 0$ is spin-unpolarized $I^S = \frac{\hbar}{2e}(I^\uparrow - I^\downarrow) \equiv 0$; (b) spin-polarized charge current $I \neq 0$ is accompanied also by spin current $I^S \neq 0$; and (c) *pure* spin current $I^S = \frac{\hbar}{2e}(I^\uparrow - I^\downarrow) \neq 0$ arising when spin- \uparrow electrons move in one direction, while an equal number of spin- \downarrow electrons move in the opposite direction, so that total charge current is $I \equiv 0$.

In this chapter we discuss how different tools of quantum transport theory, based on the nonequilibrium Green function (NEGF) techniques,² can be extended to treat spin currents and spin densities in *realistic* open paramagnetic semiconductor devices out of equilibrium. In such devices, the most important spin-dependent interaction is the SO coupling stemming from relativistic corrections to the Pauli-Schrödinger dynamics of spin- $\frac{1}{2}$ electrons. Recent theoretical efforts to understand spin transport in the presence of SO couplings by using conventional approaches, such as the bulk conductivity of infinite homogeneous systems [computed via the Kubo formula (Murakami et al., 2003; Sinova et al., 2004) or the kinetic equation (Mishchenko et al., 2004)] or spin-density³ diffusion equations for bounded

both storage and information processing on a single chip.

²The NEGF techniques for finite-size devices have been developed over the past three decades mainly through the studies of charge currents of non-interacting quasiparticles in mesoscopic semiconductor (Datta, 1995) and nanoscopic molecular (Koentopp et al., 2008) systems where quantum-coherent effects on electron transport are the dominant mechanism because of the smallness of their size. Current frontiers of the NEGF theory are also concerned with the inclusion of many-particle interaction effects responsible for dephasing (Okamoto, 2007; Thygesen and Rubio, 2008). For a lucid introduction to the general scope of NEGF formalism applied to finite-size devices see the chapter 1 by S. Datta in this Volume, as well as the chapter 23 by K. S. Thygesen and A. Rubio in the same Volume focusing on the inclusion of electronic correlations in NEGF applied to molecular junctions.

³Spin densities within the sample and spin accumulation along the sample boundaries are typically probed in recent SHE experiments on semiconductors (Kato et al., 2004a; Wunderlich et al., 2005; Sih et al., 2005,

systems (Burkov et al., 2004; Bleibaum, 2006; Galitski et al., 2006), have encountered enormous challenges even when treating non-interacting quasiparticles. Such intricacies in systems with the intrinsic SO couplings, that act homogeneously throughout the sample, can be traced to spin non-conservation due to spin precession which leads to ambiguity in defining spin currents (Shi et al., 2006; Sugimoto et al., 2006) in the bulk or ambiguity in supplying the boundary conditions for the diffusion equations (Bleibaum, 2006; Galitski et al., 2006).

On the other hand, spin-resolved NEGF techniques discussed in this chapter offer consistent description of both phase-coherent (at low temperatures) and semiclassical (at finite temperatures where dephasing takes place) coupled spin and charge transport in both clean and disordered realistic finite-size devices attached to external current and voltage probes, as encountered in experiments. The physical quantities that can be computed within this framework yield experimentally testable predictions for outflowing spin currents, induced voltages by their flow, and spin densities within the device. The presentation is tailored to be mostly of a tutorial style, introducing the essential theoretical formalism and practical computational techniques at an accessible level that should make it possible for graduate students and non-specialists in physics and engineering to engaged in theoretical and computational modeling of nanospintronic devices. We illustrate formal developments with examples drawn from the field of the *mesoscopic SHE* (Nikolić et al., 2005*b*; Sheng and Ting, 2006; Hankiewicz et al., 2004; Ren et al., 2006; Bardarson et al., 2007; Silvestrov et. al., 2009) in low-dimensional SO-coupled semiconductor nanostructures.⁴

2 WHAT IS PURE SPIN CURRENT?

Pure spin current represents flow of spin angular momentum which is not accompanied by any net charge transport [Fig. 1(c)]. They can be contrasted with traditional electronic circuits where equal number of spin- \uparrow and spin- \downarrow electrons propagate in the same direction, so that total charge current in that direction $I = I^\uparrow + I^\downarrow$ is unpolarized $I^S = 0$ [Fig. 1(a)]. Spin currents are substantially different from familiar charge currents in two key aspects: they are time-reversal invariant and they transport a vector quantity. In metal spintronic devices, ferromagnetic elements polarize electron spin thereby leading to a difference in charge currents of spin- \uparrow and spin- \downarrow electrons [Fig. 1(b)]. Such spin-polarized charge currents are accompanied by a net spin current $I^S = \frac{\hbar}{2e}(I^\uparrow - I^\downarrow) \neq 0$, as created and detected in magnetic multilayers (Maekawa and Shinjo, 2002). Figure 1 also provides a transparent illustration of one of the major advantages of pure spin currents over the spin-polarized charge currents employed by the “first-generation” spintronic devices. For example, to transport information via $2 \times \hbar/2$ spin angular momenta, Fig. 1(b) utilizes four electrons. In Fig. 1(c) the same transport of $2 \times \hbar/2$ is achieved using only two electrons moving in opposite direction. The Joule heat loss in the latter situation is only 25% of the dissipative losses in the former case.

2006).

⁴After learning about the NEGF techniques for spin transport discussed in this chapter, an interested reader might enter the field by trying to reproduce many other examples treated within this framework in our journal articles (Souma and Nikolić, 2004; Nikolić and Souma, 2005*a*; Nikolić et al., 2005*b*; Souma and Nikolić, 2005; Nikolić et al., 2005*c*, 2006; Nikolić and Zârbo, 2007; Dragomirova and Nikolić, 2007; Zârbo and Nikolić, 2007; Dragomirova et. al., 2008; Nikolić and Dragomirova, 2009; Chen et al., 2009).

3 HOW CAN PURE SPIN CURRENTS BE GENERATED AND DETECTED?

Among a plethora of imaginative theoretical proposals (Sharma, 2005; Tserkovnyak et al., 2005; Tang, 2006; Nagaosa, 2008) to generate pure spin currents using quantum effects in ferromagnet, semiconductor, and superconductor systems and their hybrids, only few have received continuous experimental attention. These include: non-local spin injection in lateral spin valves (Valenzuela and Tinkham, 2006; Kimura et al., 2007); adiabatic quantum spin pumps based on semiconductor quantum dots (Watson et al., 2003); spin current pumping by precessing magnetization of a ferromagnetic layer driven by microwaves under the ferromagnetic resonance conditions (Saitoh et al., 2006; Costache et al., 2006; Moriyama et al., 2008); optical pump-probe experiments on semiconductors (Stevens et al., 2003); and the SHE (Sih et al., 2006).

Even if spin currents are induced easily, their detection can be quite challenging since transport of electron spin between two locations in real space is alien to Maxwell electrodynamics and no “spin current ammeter” exists (Adagideli et al., 2006). In metal spintronic devices spin currents can be converted into voltage signal (Jung and Lee, 2005) by injection into ferromagnetic electrode (as achieved in lateral spin valves). On the other hand, for semiconductor spintronic devices, which do not couple well to metallic ferromagnets (Fabian et al., 2007), it is important to avoid ferromagnetic elements (and their stray fields) in both the spin injection and the spin detection processes. Multifarious theoretical ideas have been contemplated to solve this fundamental problem, ranging from the detection of tiny electric fields induced by the flow of magnetic dipoles associated with spins (Meier and Loss, 2003) to nanomechanical detection of oscillations induced by spin currents in suspended rods (Mal’shukov et al., 2005). Desirable schemes to detect pure spin current in semiconductors should exploit fundamental quantum-mechanical effects that can transform its flux into conventionally measurable voltage drops and charge currents within the same circuit through which the spin current is flowing. The recently discovered SHE holds a great promise to revolutionize generation, control, and detection of pure spin fluxes within the setting of all-electrical circuits.

4 WHAT IS THE SPIN-HALL EFFECT?

The SHE actually denotes a *collection* of phenomena manifesting as transverse separation of spin- \uparrow and spin- \downarrow states driven by longitudinally injected standard unpolarized charge current or longitudinal external electric field (Murakami, 2006; Schliemann, 2006; Sinova et al., 2006; Engel et al., 2007; Nagaosa, 2008). The spins separated in this fashion comprise either a pure spin current or accumulate at the lateral sample boundaries. Its Onsager reciprocal phenomenon—the inverse SHE (Hirsch, 1999; Hankiewicz et al., 2004, 2005; Li et al., 2006) where longitudinal pure spin current generates transverse charge current or voltage between the lateral boundaries—offers one of the most efficient schemes to detect elusive pure spin currents by converting them into electrical quantities (Valenzuela and Tinkham, 2006; Saitoh et al., 2006; Kimura et al., 2007). For an illustration of possible experimental manifestations of the direct and inverse SHE in multiterminal nanostructures see Fig. 2.

While SHE is analogous to the classical Hall effect of charges, it occurs in the absence of any

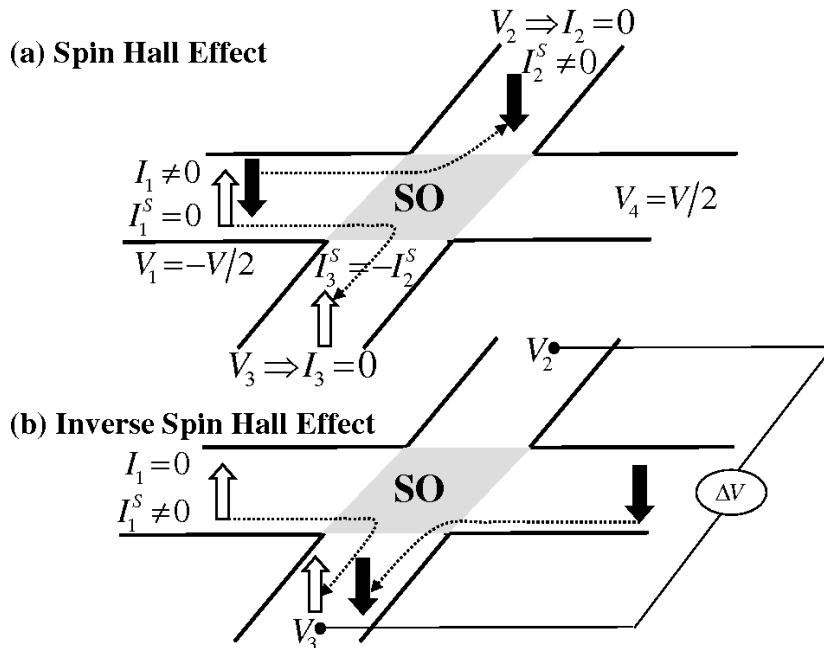


Figure 2: Basic phenomenology of the direct and inverse SHEs: (a) conventional (unpolarized) charge current flowing longitudinally through the sample experiences transverse deflection of opposite spins in opposite direction due to SO coupling induced “forces”. This generates pure spin current in the transverse direction or spin accumulation (when transverse electrodes are removed) of opposite sign at the lateral sample edges; (b) pure spin current flowing through the same sample governed by SO interactions will induce transverse charge current or voltage drop $\Delta V = V_2 - V_3$ (when transverse leads are removed). Note that to ensure purity ($I_2 = I_3 \equiv 0$) of the transverse spin-Hall current in (a), employed to define manifestations of the mesoscopic SHE in ballistic or disordered SO-coupled multiterminal nanostructures, one has to apply proper voltages V_2 and V_3 .

externally applied magnetic fields or magnetic ordering in the equilibrium state. Instead, both the direct and the inverse SHE essentially require the presence of some type of SO interactions in solids. Although SO couplings are a tiny relativistic effect for electrons in vacuum, they can be enhanced by several orders of magnitude for itinerant electrons in semiconductors due to the interplay of crystal symmetry and strong electric fields of atom cores (Winkler, 2003). They have recently emerged as one of the central paradigms (Fabian et al., 2007) of semiconductor spintronics—unlike cumbersome magnetic fields, they make possible spin control on very short length and time scales via electric fields, and could, therefore, enable smooth integration with conventional electronics.

Some of the observed SHE manifestations (Kato et al., 2004a) have been explained (Engel et al., 2007) by the SO coupling effects localized to the region around impurities which bring interplay of skew-scattering (asymmetric SO-dependent scattering which deflects spin- \uparrow and spin- \downarrow electrons of an unpolarized flux in opposite directions transverse to the flux) and side jump [due to the noncanonical nature of the physical position and velocity operators in the presence of the SO coupling around an impurity (Sinitsyn, 2008)]. These impurity-driven mechanisms were crucial ingredient of the seminal arguments in early 1970s (D’yakonov and Perel’, 1971)

predicting theoretically the existence of [in modern terminology (Hirsch, 1999)] the *extrinsic* SHE. The extrinsic SO effects are fixed by the materials properties and the corresponding SHE is hardly controllable, except through charge density and mobility (Awschalom and Flatté, 2007).

A strong impetus for the revival of interest into the realm of SHE has ascended from speculations (Murakami et al., 2003; Sinova et al., 2004) that transverse pure spin currents, several orders of magnitude larger than in the case of extrinsic SHE, can be driven by longitudinal electric fields in systems with *intrinsic* SO couplings. Such SO couplings manifest in materials with bulk inversion asymmetry or semiconductor heterostructures where inversion symmetry is broken structurally. They act homogeneously throughout the sample inducing the spin-splitting of the quasiparticle energy bands. The *intrinsic* (or band structure-driven) SHE could account for large spin current signals observed in 2D hole gases (Wunderlich et al., 2005) or huge SHE response in some metals (Guo et al., 2008). In addition, since the strength of the Rashba SO coupling (Winkler, 2003) in two-dimensional electron gases (2DEGs) within heterostructures with strong structural inversion asymmetry can be controlled experimentally by a gate electrode (Nitta et al., 1997; Grundler, 2000), intrinsically driven SHEs are amenable to easy all-electrical manipulation in realistic nanoscale multiterminal devices (Nikolić et al., 2005*b*).

The magnitude of both the extrinsic and intrinsic SHE also depends on the impurities, charge density, geometry, and dimensionality. Such a variety of SHE manifestations poses immense challenge for attempts at a unified theoretical description of spin transport in the presence of relativistic effects. This has not been resolved by early hopes (Murakami et al., 2003; Sinova et al., 2004) that auxiliary spin current density computed within infinite homogeneous systems could be elevated to universally applicable and experimentally measurable quantity (for more technical discussion of these issues see Sec. 7). Thus, theoretical analysis has increasingly been shifted toward experimentally relevant quantities in confined geometries and predictions on how to control parameters that can enhance them (Onoda and Nagaosa, 2005*a*). Examples of such quantities are edge spin accumulation (Nikolić et al., 2005*c*; Onoda and Nagaosa, 2005*a*; Nomura et al., 2005; Zyuzin et al., 2007; Silvestrov et al., 2009) and bulk spin density (Nikolić et al., 2006; Reynoso et al., 2006; Finkler et al., 2007; Chen et al., 2007; Liu et al., 2007), or outflowing spin currents driven by them (Nikolić et al., 2006).

5 WHAT IS THE MESOSCOPIC SPIN-HALL EFFECT?

Realistic devices on which SHE experiments are performed are always in contact with external electrodes and circuits which typically inject the charge current (rather than applying “longitudinal electric field”) or perform measurement of the resulting voltage drops and spatial distribution of spins and charges. In the seminal arguments (Sinova et al., 2004) for the intrinsic SHE in infinite Rashba spin-split 2DEG (in the “clean” limit), electric-field-driven acceleration of electron momenta and associated precession of spins plays a crucial role. On the other hand, mesoscopic SHE was introduced (Nikolić et al., 2005*b*) for ballistic finite-size 2DEGs attached to multiple current and voltage probes where electric field is absent in the SO-coupled central sample (on the proviso that surrounding leads are reflectionless). Another stunning difference (Sheng and Ting, 2006) between intrinsically driven SHE in the

bulk and finite-size 2DEGs is extreme sensitivity to disorder in the former case (Inoue et al., 2004) which, for linear in momentum SO couplings (such as the Rashba one), is able to completely destroy the spin-Hall current density in unbounded systems (Mishchenko et al., 2004; Adagideli and Bauer, 2005). Unlike in three-dimensional semiconductor and metallic devices, which are always disordered and where extrinsic contribution to the SHE is therefore present or dominant, ballistic conditions for the mesoscopic SHE can be achieved in low-dimensional semiconductor systems. In fact, the very recent experiment on nanoscale H-shaped structures realized using high mobility HgTe/HgCdTe quantum wells has reported for the first time the detection of mesoscopic SHE via non-local and purely electrical measurements (Brüne et al., 2008).

The magnitude of pure spin currents flowing out of mesoscopic SHE device (illustrated in Fig. 2) through ideal (spin and charge interaction free) electrodes is governed by the spin precession length L_{SO} . This mesoscopic length scale (e.g., $L_{SO} \sim 100$ nm in recently fabricated 2DEGs), on which the vector of the expectation values of spin precesses by an angle π , has been identified through intuitive physical arguments (Engel et al., 2007) as an important parameter for spin distributions (e.g., in clean systems the spin response to inhomogeneous field diverges at the wave vector $q = 2/L_{SO}$). In fact, the mesoscopic SHE analysis predicts (Nikolić et al., 2005*b*) via numerically exact calculations (see Fig. 8) that optimal device size for achieving large spin currents is indeed $L \simeq L_{SO}$. This is further confirmed by alternative analyses of the SHE response in finite-size systems (Moca and Marinescu, 2007). In the general cases (Sih et al., 2005; Hankiewicz and Vignale, 2008), where both the extrinsic and intrinsic SO interaction effects are present, the intrinsically driven contribution to SHE in finite-size devices dominates (Nikolić and Zârbo, 2007) when the ratio of characteristic energy scales (Nagaosa, 2008) for the disorder and SO coupling effects satisfies $\Delta_{SO}\tau/\hbar \gtrsim 1$ (Δ_{SO} is the spin-splitting of quasiparticle energies and \hbar/τ is the disorder induced broadening of energy levels due to transport scattering time τ).

For mesoscopic SHE devices in the phase-coherent transport regime (device smaller than the dephasing length), one can also observe the effects of quantum confinement and quantum interferences in spin-related quantities that counterpart familiar examples from mesoscopic charge transport (Datta, 1995). They include: SHE conductance fluctuations (Ren et al., 2006; Bardarson et al., 2007); resonances in SHE conductance due to opening of new conducting channels (Nikolić et al., 2005*b*; Sheng and Ting, 2006) or mixing of bound (Bulgakov et al., 1999) and propagating states due to SO couplings; and constructive or destructive quantum interference-based control (Souma and Nikolić, 2005) of spin-Hall current in multiterminal Aharonov-Casher rings (as the electromagnetic dual of Aharonov-Bohm rings where SO coupling, rather than magnetic field, permeates the ring). The charge and spin dephasing can be included (Golizadeh-Mojarad and Datta, 2007*a*) within the same NEGF transport formalism to allow for comparison with experiments performed at finite temperatures where quantum coherence effects are smeared out (Golizadeh-Mojarad and Datta, 2007*b*).

In general, the presence of SO couplings requires to treat the whole device geometry when studying the dynamics of transported spin densities. For example, the decay of nonequilibrium spin polarizations in ballistic or disordered quantum wires is highly dependent on the transverse confinement effects (Nikolić and Souma, 2005*a*; Holleitner et al., 2006) or chaotic vs. regular boundaries of quantum dots (Chang et al., 2004). Since SO couplings in SHE

devices manifest through both of their aspects—creation of spin currents and concurrently relaxation of spins—it is a nontrivial task to understand how spin currents and edge spin accumulations scale with increasing the strength of the SO couplings (Onoda and Nagaosa, 2005a).

The analysis of the whole device setup, where central SO-coupled sample is treated together with the surrounding electrodes, also simplifies the discussion of esoteric SHE concepts, such as the SHE in insulators (Onoda and Nagaosa, 2005b) [where electrodes introduce dissipation necessary to obtain nonzero value of spin accumulation as time-reversal odd quantity] or quantum SHE (König et al., 2008) whose quantized spin-Hall conductance is due to chiral spin-filtered (or helical) edge states (i.e., Kramers doublets of states forcing electrons of opposite spin to flow in opposite directions along the edges of the sample) in a multiterminal SO-coupled bridge with energy gap in the central sample (Sheng et al., 2005). For example, recent direct experimental evidence (Roth et al., 2009) for nonlocal transport in HgTe quantum wells in the quantum spin-Hall regime, which shows how non-dissipative quantum transport occurs through chiral spin-filtered edge states while the contacts lead to equilibration between the counter-propagating spin states at the edge, can be analyzed only by the device-oriented quantum transport techniques discussed in this chapter.

6 SO COUPLINGS IN LOW-DIMENSIONAL SEMI-CONDUCTORS

The coupling between the orbital and the spin degree of freedom of electrons is a relativistic effect described formally by the nonrelativistic expansion of the Dirac equation in external electric and magnetic fields (for which exact solutions do not exist) in powers of the inverse speed of light c . In the second order v^2/c^2 , one identifies (Zawadzki, 2005) the SO term⁵

$$\hat{H}_{\text{SO}} = \frac{\hbar}{4m_0^2c^2} \hat{\mathbf{p}} \cdot (\hat{\boldsymbol{\sigma}} \times \nabla V(\mathbf{r})), \quad (1)$$

responsible for the entanglement of the spin and orbital degrees of freedom in the two-component nonrelativistic Pauli Hamiltonian for spin- $\frac{1}{2}$ electron. Here m_0 is the free electron mass, $\hat{\boldsymbol{\sigma}} = (\hat{\sigma}_x, \hat{\sigma}_y, \hat{\sigma}_z)$ is the vector of the Pauli matrices, and $V(\mathbf{r})$ is the electric potential. The SO coupling term can also be extracted from the semiclassical analysis that usually invokes the interaction of the electron magnetic dipole moment (associated with spin) with magnetic field in the frame moving with electron (Jackson, 1998). In the instantaneous rest frame of an electron, magnetic field is obtained by Lorentz transforming electric field from the laboratory frame. It is actually more efficient for intuitive analysis of different experimental situations to remain (Fisher, 1971) in the laboratory frame where a magnetic dipole $\boldsymbol{\mu}$ moving with velocity \mathbf{v} generates electric dipole moment

$$\mathbf{P}_{\text{lab}} = \mathbf{v} \times \boldsymbol{\mu}/c^2. \quad (2)$$

⁵Although a topic of numerous textbooks on relativistic quantum mechanics and quantum field theory, the v^2/c^2 expansion has recently been carefully reexamined (Zawadzki, 2005) to find all terms at this order of approximation in manifestly gauge invariant form, thereby revealing various inconsistencies in the textbook literature.

Here the right-hand side is evaluated in the electron rest frame and \mathbf{P}_{lab} is measured in the lab (both sides can be evaluated in the lab yielding the same result to first order in v/c). The potential energy of the interaction of the electric dipole with the external electric field \mathbf{E}_{lab} in the lab frame, $U_{\text{dipole}} = -\mathbf{P}_{\text{lab}} \cdot \mathbf{E}_{\text{lab}}$, corrected to the Thomas precession⁶ $U_{\text{Thomas}} = -U_{\text{dipole}}/2$ leads to the SO coupling term $U_{\text{SO}} = U_{\text{dipole}} + U_{\text{Thomas}} = -\mathbf{P}_{\text{lab}} \cdot \mathbf{E}_{\text{lab}}/2$.

The lab frame analysis allows one to quickly depict the Mott skew-scattering off a target whose Coulomb field deflects a beam of spin- \uparrow and spin- \downarrow particles in opposite directions, thereby, e.g., polarizing the beam of neutrons (Fisher, 1971) or generating skew-scattering contribution (Engel et al., 2007; Hankiewicz and Vignale, 2008) to the extrinsic SHE. For example, if we look at spin- \uparrow electron from behind moving along the y -axis, whose expectation value of the spin vector is oriented along the positive z -axis so that the corresponding magnetic dipole moment lies along the negative z -axis, then in the lab frame we also see its Lorentz transformed electric dipole moment \mathbf{P}_{lab} oriented along the negative x -axis. The electric dipole feels the force $\mathbf{F} = (\mathbf{P}_{\text{lab}} \cdot \nabla) \mathbf{E}_{\text{lab}}$, oriented in this case along the positive x -axis (right transverse direction with respect to the motion of the incoming electron) since gradient of the electric field \mathbf{E}_{lab} generated by the target is always negative outside of it. Note that this simple-minded classical picture only explains one aspect of the SO-dependent interaction with impurity. The other one—the so-called side jump (i.e., sideways shift of the scattering wave packet)—requires more quantum mechanical analysis (Sinitsyn, 2008) to extract additional contribution to the velocity operator due to impurity potential $V_{\text{disorder}}(\mathbf{r})$ in the SO Hamiltonian Eq. (1).

The heuristic discussion based on the Lorentz transformations gives only a minuscule effect and the influence of electronic band structure is essential (Engel et al., 2007) to make these effects experimentally observable in solids. In the case of atoms, SO coupling is due to interaction of electron spin with the average Coulomb field of the nuclei and other electrons. In solids, $V(\mathbf{r})$ is the sum of periodic crystalline potential and an aperiodic part containing potentials due to impurities, confinement, boundaries and external electric fields. The nonrelativistic expansion of the Dirac equation can be viewed as a method of systematically including the effects of the negative-energy solutions on the positive energy states starting from their nonrelativistic limit (Zawadzki, 2005). This effect in vacuum is small due to huge gap $2m_0c^2$ between positive and negative energy states. In solids, strong nuclear potential competes with this huge denominator in Eq. (1), so that much smaller band gap between conduction and valence band (playing the role of electron positive energy sea and positron negative energy sea, respectively) replaces $2m_0c^2$, thereby illustrating the origin of strong enhancement of the SO couplings in solids (Winkler, 2003).

Although intrinsic SO couplings can always be written in the Zeeman form $\hat{\sigma} \cdot \mathbf{B}_{\text{SO}}(\mathbf{p})$, their effective magnetic field $\mathbf{B}_{\text{SO}}(\mathbf{p})$ is momentum-dependent and, therefore, does not break the time-reversal invariance. The Kramers theorem (Ballentine, 1998) for time-reversal invariant quantum systems requires that the energy bands $\varepsilon_n(\mathbf{k})$ of an electron in a periodic potential satisfy $\varepsilon_n(\mathbf{k}, \uparrow) = \varepsilon_n(-\mathbf{k}, \downarrow)$ since $\mathbf{k} \mapsto -\mathbf{k}$ and $\sigma = \uparrow \mapsto \sigma = \downarrow$ upon time reversal ($\hbar\mathbf{k}$ is crystal momentum). Therefore, in semiconductors invariant under spatial inversion $\mathbf{k} \mapsto -\mathbf{k}$ (such as silicon) the Kramers theorem gives double degenerate spin states for any \mathbf{k} value, $\varepsilon_n(\mathbf{k}, \uparrow) = \varepsilon_n(\mathbf{k}, \downarrow)$. To obtain a non-zero $\mathbf{B}_{\text{SO}}(\mathbf{p})$ that breaks the spin degeneracy

⁶The Thomas precession takes into account change in rotational kinetic energy due to the precession of the accelerated electron as seen by laboratory observer in the “extended” special relativity of accelerated objects.

in three-dimensional crystals $\varepsilon_n(\mathbf{k}, \uparrow) \neq \varepsilon_n(\mathbf{k}, \downarrow)$ the host crystal has to be inversion asymmetric. In bulk semiconductors with zinc-blende symmetry, the conduction band of III-V compounds will split into two subbands where anisotropic spin-splitting is proportional to k^3 . Such SO-induced splitting is termed cubic Dresselhaus SO coupling, and it is associated with bulk inversion asymmetry (BIA). In semiconductor heterostructures (Winkler, 2003), ideal symmetry of the 3D host crystal is broken by the interface where 2DEG or two-dimensional hole gas (2DHG) is confined within a quantum well. In such reduced effective dimensionality, the symmetry of the underlying crystal lattice is lowered, so that an additional linear in k Dresselhaus term becomes relevant. Besides microscopic crystalline potential $V_{\text{crystal}}(\mathbf{r})$ as the source of the electric field in the SO coupling term in Eq. (1), an interface electric field accompanying the quantum well structural inversion asymmetry (SIA) gives rise to the Rashba spin-splitting of conduction band electrons

$$\hat{H}_{\text{Rashba}} = \frac{\alpha}{\hbar}(\hat{\boldsymbol{\sigma}} \times \hat{\mathbf{p}}) \cdot \hat{\mathbf{e}}_z, \quad (3)$$

for 2DEG in the xy -plane and $\hat{\mathbf{e}}_z$ as the unit vector along the z -axis. In narrow gap semiconductors the Rashba effect linear in k should dominate over the bulk k^3 Dresselhaus term. Moreover, it has been experimentally demonstrated that Rashba coupling can be changed by as much as 50% by external gate electrode (Nitta et al., 1997; Grundler, 2000) covering 2DEG, which has become one of the key concepts in semiconductor spintronics. Nevertheless, there is a lengthy theoretical debate on the importance of different electric field contributions to the value of experimentally observed α and the parameters which are effectively manipulated via the gate electrode to cause its increase (Grunbler, 2000)—we refer to a comprehensive overview of these issues by Fabian et al. (2007) and Winkler (2003). Note that impurity determined $V_{\text{disorder}}(\mathbf{r})$ contribution to Eq. (1) does not require broken inversion asymmetry of the pure crystal or of the structure.

The coupling between electron momentum and spin correlates charge currents and spin densities in SO-coupled semiconductors (Silsbee, 2004) leading to highly non-trivial effects in nonequilibrium situations. Some of these have been observed in recent magneto-electric experiments (Ganichev et al., 2006; Silov et al., 2004; Kato et al., 2004b), where charge current induces spin density, as well as in the spin galvanic experiments (Ganichev and Prettl, 2003), where nonequilibrium spin density drives a charge current. It is also the key ingredient of intrinsically driven SHEs [where the induced spin density is oriented out-of-plane, rather than in-plane as in the magneto-electric effects (Silsbee, 2004)].

In this Section we focus on the description of the Rashba SO coupling⁷ in the form suitable for spin-dependent NEGF calculations using local orbital basis and the lattice Hamiltonian defined by it. The Rashba Hamiltonian prepared in this fashion will be used as the starting point for illustrating SHE-related spin and charge transport calculations in Sec. 8. We also add the treatment of the extrinsic SO coupling in 2DEG within the same local orbital basis framework in Sec. 6.3.2 to enable the description of the most general experimental situations (Sih et al., 2005) in low-dimensional devices where both extrinsic and intrinsic mechanisms can act concurrently (Nikolić and Zârbo, 2007; Hankiewicz and Vignale, 2008; Dragomirova et al., 2008).

⁷The same analysis applies to linear Dresselhaus coupling since they can be transformed into each other by a unitary matrix.

6.1 Rashba coupling in bulk 2DEG

The effective single-particle SO Hamiltonian for a clean infinite homogeneous 2DEG with the Rashba coupling Eq. (3) can be formally rewritten as

$$\hat{H}_R^{2D} = \frac{\hat{\mathbf{p}}^2}{2m^*} \otimes \mathbf{I}_S + \frac{\alpha}{\hbar} (\hat{p}_y \otimes \hat{\sigma}_x - \hat{p}_x \otimes \hat{\sigma}_y). \quad (4)$$

Here \otimes stands for the tensor product of two operators acting in the tensor product $\mathcal{H}_O \otimes \mathcal{H}_S$ of the orbital and spin Hilbert spaces, and m^* is the effective mass. To enforce pedagogical notation, we also use \mathbf{I}_O as the unit operator in \mathcal{H}_O and \mathbf{I}_S for the unit operator in \mathcal{H}_S . The internal *momentum-dependent* magnetic field corresponding to the Rashba coupling is extracted from Eq. (3), recast in the form of the Zeeman term $-g\mu_B \hat{\boldsymbol{\sigma}} \cdot \mathbf{B}_R(\mathbf{p})/2$, as $\mathbf{B}_R(\mathbf{p}) = (2\alpha/g\mu_B) (\mathbf{p} \times \mathbf{e}_z)$. The Hamiltonian commutes with the momentum operator $\hat{\mathbf{p}}$, time-reversal operator \hat{T} , and the chirality operator $(\hat{\boldsymbol{\sigma}} \times \hat{\mathbf{p}}/|\mathbf{p}|) \cdot \mathbf{e}_z$. The zero commutator $[\hat{H}, \hat{\mathbf{p}}] = 0$ due to the translation invariance of infinite 2DEG implies that solutions of the Schrödinger equation are of the form

$$\Psi(\mathbf{r}) = C e^{i\mathbf{k}\mathbf{r}} |\chi\rangle_s, \quad (5)$$

where $|\chi\rangle_s$ is a two-component spinor. Due to time-reversal invariance $[\hat{H}, \hat{T}] = 0$, the two eigenstates of opposite momenta and spins are degenerate, $E(\mathbf{k}, \sigma) = E(-\mathbf{k}, -\sigma)$. The time-reversal operator can be written as $\hat{T} = \hat{K} \otimes \exp(i\pi \hat{\sigma}_y/2)$, where \hat{K} is the complex conjugation operator (Ballentine, 1998). If the Hamiltonian is invariant to chirality transformation, the spin state is momentum-dependent. In the Rashba case the spin and momentum of an eigenstate are always perpendicular to each other.

The Rashba Hamiltonian Eq. (4) in the case of a 1D electron gas (1DEG) reduces to

$$\hat{H}_R^{1D}(k_x) = \frac{\hbar^2 k_x^2}{2m^*} - \alpha k_x \hat{\sigma}_y. \quad (6)$$

Its eigenvalues define the energy-momentum dispersion

$$E_{\pm}(k_x) = \frac{\hbar^2 k_x^2}{2m^*} \pm \alpha |k_x|, \quad (7)$$

with the corresponding eigenvectors

$$\psi_{k_x, \pm} = \frac{e^{ik_x x}}{\sqrt{2\pi\hbar}} \cdot \frac{1}{\sqrt{2}} \begin{pmatrix} 1 \\ \mp i \frac{k_x}{|k_x|} \end{pmatrix}. \quad (8)$$

These eigenstates are labeled with the momentum operator eigenvalue $\hbar k_x$ and the chirality operator eigenvalue $\lambda = \pm 1$. Equation (8) shows that

$$\langle \psi_{k_x, \pm} | \hat{\sigma}_y | \psi_{k_x, \pm} \rangle = \mp \frac{k_x}{|k_x|}, \quad (9)$$

meaning that each spin-split parabolic subband has a well-defined spin.

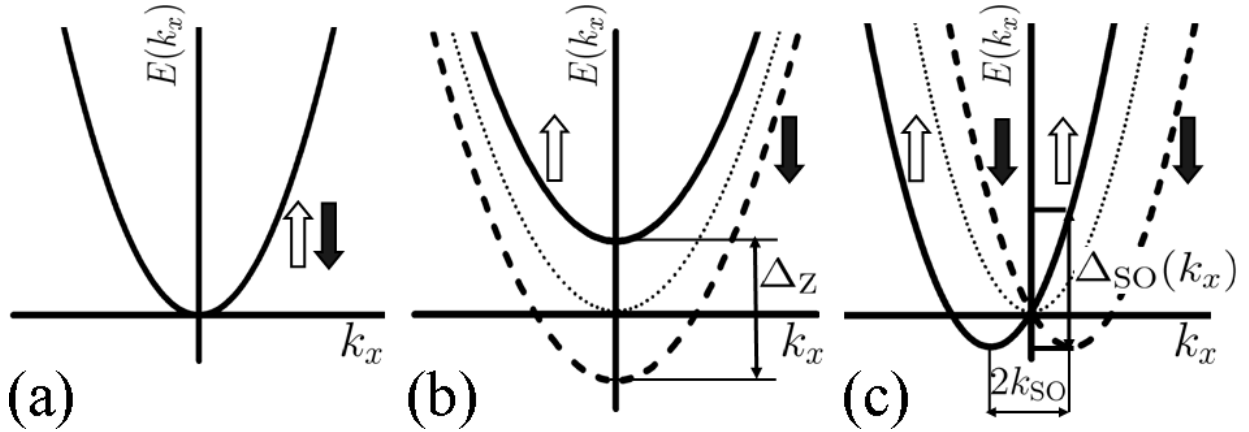


Figure 3: The one-dimensional energy-momentum dispersion for: a) infinite clean 1DEG, b) 1DEG in magnetic field, and c) 1DEG with the Rashba SO coupling. The SO-induced spin splitting in (c) is signified by the energy separation Δ_{SO} at a given k_x . The complementary description of the SO-induced spin splitting is k_{SO} difference between the momenta of two electrons of opposite spins and chiralities in panel (c).

To elucidate the physical meaning of the SO-induced spin splitting, we compare in Fig. 3 the Rashba dispersion with more familiar Zeeman splitting of 1DEG placed in the external (momentum-independent) magnetic field. In the case of the Zeeman splitting, the spin- \uparrow and spin- \downarrow subbands are shifted vertically with respect to each other by the Zeeman energy Δ_Z . On the other hand, the Rashba spin-splitting depends on momentum

$$\Delta_{\text{SO}}(k_x) = 2\alpha k_x, \quad (10)$$

so that $E_+(k_x)$ and $E_-(k_x)$ are shifted horizontally along the momentum axis rather than along the energy axis. This ensures that the system remains spin-unpolarized in equilibrium, as dictated by the time-reversal invariance and the fact that spin density is time-reversal odd quantity. The spin splitting can also be described using k_{SO} as the difference between the momenta of two electrons of opposite spins and chiralities, and different experiments (such as Shubnikov-de Haas, Raman scattering, or spin precession) probe either Δ_{SO} or k_{SO} illustrated in Fig. 3(c).

From Eq. (9) we see that the y -component of spin of the eigenstate $|\psi_{k_x, \lambda}\rangle$ is \uparrow for $\lambda = 1$ and k_x negative, and \downarrow for $\lambda = -1$ and k_x positive. The opposite is true for the other branch $E_{\lambda=-1}(k_x)$. Thus, the eigenvalues of spin $\hat{\sigma}_y$ are good quantum numbers since in 1D $\hat{\sigma}_y$ commutes with the Hamiltonian. Following this argument, it is easy to understand the relative spin orientations of the states along each of the dispersion branches.

As in 1D case, the Rashba Hamiltonian in 2D commutes with momentum, chirality, and the time-reversal operator. Its eigenenergies

$$E_{\pm}(\mathbf{k}) = \frac{\hbar^2 \mathbf{k}^2}{2m^*} \pm \alpha |\mathbf{k}|, \quad (11)$$

are plotted in Fig. 4. They are labeled by a 2D wave vector $|\mathbf{k}| = \sqrt{k_x^2 + k_y^2}$ and the chirality eigenvalues $\lambda = \pm 1$ (i.e., the spin projection perpendicular to both \mathbf{k} and growth direction

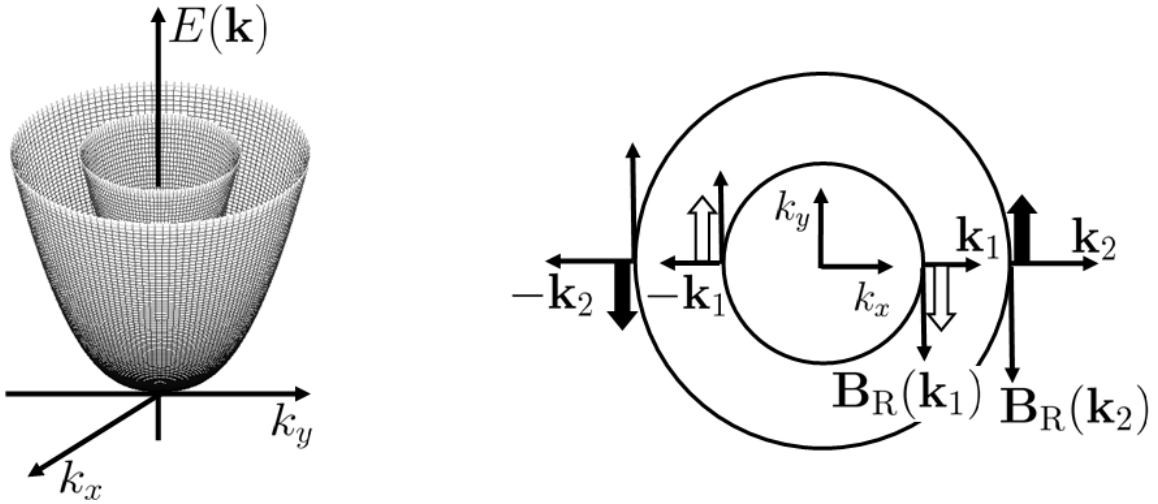


Figure 4: The energy-momentum dispersion $E(k_x, k_y)$ of the Rashba spin-split 2DEG. The states at the Fermi level lie on two concentric Fermi circles, $E_+(\mathbf{k}) = E_F$ for the inner circle and $E_-(\mathbf{k}) = E_F$ for the outer circle, as shown in the right panel. The radius of the inner circle is k_1 and the radius of the outer one is denoted by k_2 . The Fermi momentum k_F of the free particle is $k_1 \leq k_F \leq k_2$. For a given momentum \mathbf{k} , the spin of an electron is oriented either parallel [$E_+(\mathbf{k})$ branch] or anti-parallel [$E_-(\mathbf{k})$ branch] to the momentum-dependent effective magnetic field $\mathbf{B}_R(\mathbf{k})$. The states of opposite momentum and spin on each Fermi circle are Kramers degenerate.

along the z -axis). The corresponding eigenstates are

$$\psi_{\mathbf{k},\pm} = \frac{e^{i\mathbf{k}\mathbf{r}}}{2\pi\hbar} \cdot \frac{1}{\sqrt{2}} \begin{pmatrix} 1 \\ \pm \frac{k_y - ik_x}{|\mathbf{k}|} \end{pmatrix}. \quad (12)$$

Finding the expectation value of the spin operator $\hbar\hat{\sigma}/2$ in eigenstate Eq. (12)

$$\langle \psi_{\mathbf{k},\pm} | \hat{\sigma} | \psi_{\mathbf{k},\pm} \rangle = \pm \frac{k_y}{|\mathbf{k}|} \mathbf{e}_x \mp \frac{k_x}{|\mathbf{k}|} \mathbf{e}_y, \quad (13)$$

demonstrates (Winkler, 2003) that no common spin quantization axis can be found for all eigenstates of the Rashba spin-split 2DEG (\mathbf{e}_x and \mathbf{e}_y are the unit vectors within the xy -plane of 2DEG).

6.2 Rashba coupling in quantum wires

6.2.1 Energy dispersion of Rashba spin-split transverse propagating subbands

The Rashba Hamiltonian for a quantum wire patterned within 2DEG (along the x -axis)

$$\hat{H}_R^{\text{Q1D}} = \frac{\hat{\mathbf{p}}^2}{2m^*} + \frac{\alpha}{\hbar} (\hat{\sigma} \times \hat{\mathbf{p}}) \cdot \mathbf{z} + V_{\text{conf}}(y), \quad (14)$$

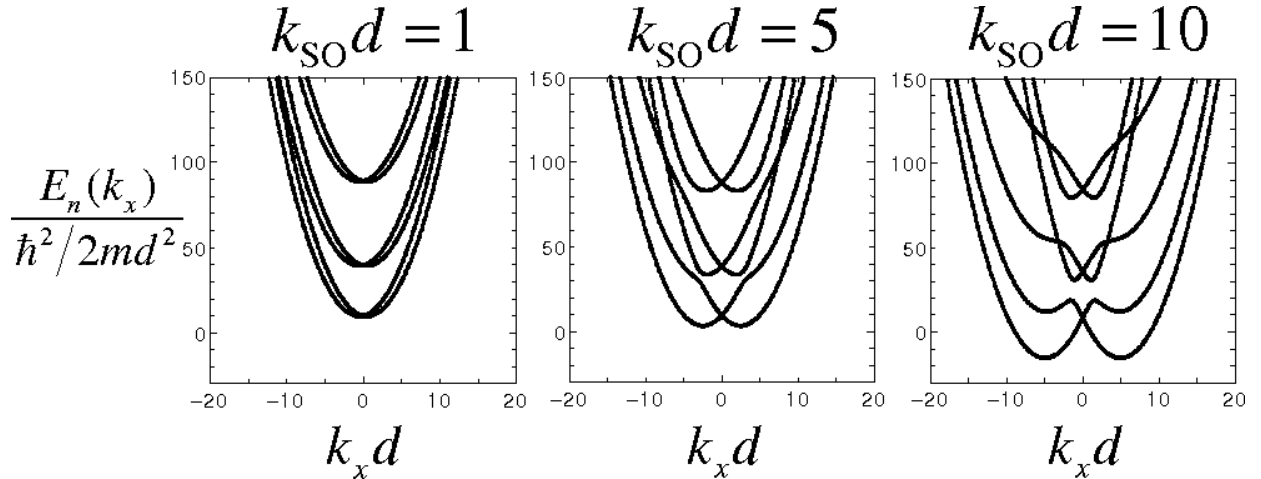


Figure 5: The subband energy-momentum dispersion in the Rashba spin-split clean quantum wire. The parameter $k_{\text{SO}}d$ (d is the width of the wire) defines the weak and strong SO coupling regimes. For large values of $k_{\text{SO}}d$ the mixing of subbands is nontrivial giving rise to strong energy dependence of the wire conductance.

describes quasi-one-dimensional electron gas (Q1DEG) of width d whose lateral confinement is accounted by the potential $V_{\text{conf}}(y)$. The motion along the confinement direction is quantized, such that the energy-momentum dispersion in the absence of SO coupling is split into spin degenerate quasi 1D subbands with quadratic dispersion $E_{\pm}(k_x) = E_n + \hbar^2 k_x^2 / 2m^*$ in 1D wave vector k_x labeling an eigenstate of the subband with index n . The effective mass Rashba Hamiltonian for a quantum wire is translationally invariant along wire direction x , and can be separated into three terms $\hat{H} = \hat{H}_{\text{sb}} + \hat{H}_{\text{mix}} + \hat{H}_{\text{1D}}$ (Governale and Zülicke, 2004):

$$\hat{H}_{\text{sb}} = \frac{\hat{p}_y^2}{2m^*} + V_{\text{conf}}(y), \quad (15a)$$

$$\hat{H}_{\text{mix}} = -\frac{\hbar k_{\text{SO}}}{m^*} \hat{\sigma}_x \hat{p}_y, \quad (15b)$$

$$\hat{H}_{\text{1D}} = \frac{\hbar^2}{2m^*} (k_x + k_{\text{SO}} \hat{\sigma}_y)^2 + \frac{\hbar^2 k_{\text{SO}}^2}{2m^*}. \quad (15c)$$

The term \hat{H}_{sb} defines the eigenenergies E_n of the transverse confining potential, while \hat{H}_{1D} is the 1D translationally invariant Rashba term for the quantum wire. Therefore, in the hypothetical case where the second term \hat{H}_{mix} is absent, the eigenenergies of the Hamiltonian Eq. (15) show only k_x -dependent splitting

$$E_{\pm}(k_x) = E_n + \frac{\hbar^2 k_x^2}{2m^*} \pm \alpha |k_x|. \quad (16)$$

When the expectation values E_{mix} of \hat{H}_{mix} between the eigenstates of $\hat{H}_{\text{sb}} + \hat{H}_{\text{1D}}$ are of the order of $\Delta E_n = E_{n+1} - E_n$, the mixing of the spin-split subbands becomes important. Thus, the ratio

$$\frac{E_{\text{mix}}}{\Delta E_n} \simeq \frac{\hbar k_{\text{SO}}}{m^*} \frac{\pi \hbar}{d} \left(\frac{\pi^2 \hbar^2}{m^* d^2} \right)^{-1} = \frac{d}{L_{\text{SO}}} = \frac{k_{\text{SO}} d}{\pi}, \quad (17)$$

gives a simple criterion to separate the strong and weak SO coupling regimes in Q1DEGs. In the weak coupling regime $L_{\text{SO}} \gg d$ the subband mixing is negligible, as illustrated in Fig. 5(a). In quantum wires with strong Rashba effect, realized for $L_{\text{SO}} \lesssim d$ (or $k_{\text{SO}}d \gtrsim \pi$) hybridization of quasi-1D subbands becomes important and Eq. (16) can not capture the non-parabolic energy dispersions in Fig. 5(b),(c). Unlike the weak coupling regime where the Hamiltonian eigenstates are also eigenstates of $\hat{\sigma}_y$ (i.e., their spins are polarized in-plane along the y -axis), in the strong coupling regime no common spin quantum number can be assigned to states within a given subband (Governale and Zülicke, 2004).

6.2.2 Spin precession in Rashba quantum wires

The lifting of spin degeneracy of each transverse subband of a quantum wire by the Rashba coupling means that an electron injected at the Fermi energy E_F can have two different wave vectors within the wire, $E_+(k_{x1}) = E_-(k_{x2}) = E_F$. The wave vector k_{x1} labels the eigenstates of E_+ spin-split subband whose spinor part is $\frac{1}{\sqrt{2}} \begin{pmatrix} 1 \\ i \end{pmatrix}$ [describing spin- \uparrow along the y -axis], while k_{x2} labels the eigenstates of E_- subband associated with the eigenspinor $\frac{1}{\sqrt{2}} \begin{pmatrix} 1 \\ -i \end{pmatrix}$ [describing spin- \downarrow along the y -axis]. Thus, when electron with spin- \uparrow along the z -axis is injected from a half-metallic ferromagnet into the Rashba quantum wire, as proposed in the Datta-Das spin-FET device (Datta and Das, 1990), the outgoing wave function from a wire of length L will be

$$\psi(L) \sim e^{ik_{x1}L} \begin{pmatrix} 1 \\ i \end{pmatrix} + e^{ik_{x2}L} \begin{pmatrix} 1 \\ -i \end{pmatrix}. \quad (18)$$

The probability to detect a particle with spin- \uparrow or with spin \downarrow along the z -axis is given by

$$|\langle (1 \ 0) | \psi(L) \rangle| = 4 \cos^2 \frac{(k_{x1} - k_{x2})L}{2}, \quad (19a)$$

and

$$|\langle (0 \ 1) | \psi(L) \rangle| = 4 \sin^2 \frac{(k_{x1} - k_{x2})L}{2}, \quad (19b)$$

respectively. Such modulation of current by spin precession with angle $\Delta\theta = \Delta k_x L$, where $\Delta k_x = k_{x2} - k_{x1} = 2m^*\alpha/\hbar^2$ stems from $E_+(k_{x2}) - E_-(k_{x1}) = 0$, would provide the basis for the operation of the envisioned spin-FET device (Datta and Das, 1990). It also introduces in a transparent fashion the concept of the *spin precession length*

$$L_{\text{SO}} = \frac{\pi\hbar^2}{2m^*\alpha}, \quad (20)$$

along which the vector of the expectation values of spin precesses by an angle $\Delta\theta = \pi$ while propagating along the Rashba wire.

We emphasize that the energy independence of L_{SO} holds for weak SO coupling and narrow wires. As discussed in Sec. 6.2.1, for strong SO coupling $d > L_{\text{SO}}$, intersubband mixing becomes important, so that Eq. (20) is inapplicable. The L_{SO} scale appears as the characteristic length scales for various processes in semiconductor spintronic systems. For example, in weakly disordered systems L_{SO} also plays the role of a characteristic scale for the D'yakonov-Perel' spin dephasing where nonequilibrium spin density decays due to randomization of $\mathbf{B}_R(\mathbf{p})$ in each scattering event changing \mathbf{p} and, therefore, the direction of magnetic field

around which spin precesses (Chang et al., 2004; Fabian et al., 2007). It also sets a mesoscopic scale [~ 100 nm in heterostructures with large α (Nitta et al., 1997; Grundler, 2000)] at which one can expect the largest SHE response (Nikolić et al., 2005*b*, 2006; Moca and Marinescu, 2007).

6.3 Discrete representation of effective SO Hamiltonians

In order to perform numerical calculations on finite-size systems of arbitrary shape attached to external electrodes it is highly advantageous to discretize the effective SO Hamiltonian. Here we introduce a discretization scheme for the Rashba Hamiltonian. In addition, we also discuss discretization scheme for the extrinsic SO Hamiltonian which makes it possible to treat intrinsic and extrinsic SO coupling effect on equal footing in nanostructures (Nikolić and Zárbo, 2007; Dragomirova et. al., 2008).

The grid used for discretization is collection of points $\mathbf{m} = (m_x, m_y)$ on a square lattice of constant a , where m_x, m_y are integers. We use the following notation: $\psi_{\mathbf{m}} \equiv \langle \mathbf{m} | \psi \rangle$ for the wave function evaluated at point \mathbf{m} ; and $A_{\mathbf{m}\mathbf{m}'} \equiv \langle \mathbf{m} | \hat{A} | \mathbf{m}' \rangle$ for the matrix element of an operator \hat{A} . In finite difference methods, one has to evaluate the derivatives of a function $f(x)$ on a grid $\{\dots, x_{m-1}, x_m, x_{m+1}, \dots\} \equiv \{\dots, (m-1)a, ma, (m+1)a, \dots\}$:

$$\left(\frac{df}{dx}\right)_m = \frac{f_{m+1} - f_{m-1}}{2a}, \quad (21)$$

where $f_m \equiv f(x_m)$. The second derivative can be computed as

$$\left(\frac{d^2f}{dx^2}\right)_m = \frac{f_{m+1} - 2f_m + f_{m-1}}{a^2}. \quad (22)$$

For a particular discretization scheme, the matrix elements of the derivative operators can be expressed in the local orbital basis $|m\rangle$, which can be interpreted as each site hosting a single s -orbitals as in the tight-binding models of solids. For instance, using Eq. (21) we get

$$\left\langle m \left| \frac{d}{dx} \right| n \right\rangle = \frac{\langle m+1 | n \rangle - \langle m-1 | n \rangle}{2a} = \frac{\delta_{n,m+1} - \delta_{n,m-1}}{2a}, \quad (23)$$

where δ is the Kronecker symbol. The same can be done for the operator d^2/dx^2 using Eq. (22)

$$\begin{aligned} \left\langle m \left| \frac{d^2}{dx^2} \right| n \right\rangle &= \frac{\langle m+1 | n \rangle - 2\langle m | n \rangle + \langle m-1 | n \rangle}{a^2} \\ &= \frac{\delta_{n,m+1} - 2\delta_{n,m} + \delta_{n,m-1}}{a^2}. \end{aligned} \quad (24)$$

It is worth mentioning that for a given grid, the differentiation operators matrix elements are dependent on the discretization scheme used. For example, if Eq. (23) is used to get $d^2/dx^2 = d/dx \cdot d/dx$ it would lead to a different result than the one in Eq. (24). This is due to the fact that these matrix elements are not computed but approximated, and this depends on the selected discretization scheme.

The discrete one-particle operators are written in the second quantized notation as

$$\hat{A} = \sum_{m,n} \langle m | \hat{A} | n \rangle \hat{c}_m^\dagger \hat{c}_n, \quad (25)$$

which, together with Eqs. (23), (24), leads to

$$\frac{d}{dx} = \sum_m \frac{1}{2a} (\hat{c}_m^\dagger \hat{c}_{m+1} - \hat{c}_m^\dagger \hat{c}_{m-1}), \quad (26a)$$

$$\frac{d^2}{dx^2} = \sum_m \frac{1}{a^2} (\hat{c}_m^\dagger \hat{c}_{m+1} - 2\hat{c}_m^\dagger \hat{c}_m + \hat{c}_m^\dagger \hat{c}_{m-1}). \quad (26b)$$

Equations (26a), (26b) can be used to discretize the effective mass Hamiltonian of a quasi-electron in the clean spin and charge interaction-free 2DEG

$$\hat{H}_{\text{free}} = \frac{\hat{\mathbf{p}}^2}{2m^*} \otimes \mathbf{I}_S = -\frac{\hbar^2}{2m^*} \left(\frac{\partial^2}{\partial x^2} + \frac{\partial^2}{\partial y^2} \right) \otimes \mathbf{I}_S, \quad (27)$$

where the discretized version of the same Hamiltonian is

$$\hat{H}_{\text{free}} = \sum_{\mathbf{m}\mathbf{m}'\sigma} t_{\mathbf{m}\mathbf{m}'} \hat{c}_{\mathbf{m}\sigma}^\dagger \hat{c}_{\mathbf{m}'\sigma}. \quad (28)$$

This is familiar tight-binding Hamiltonian on the square lattice with single s -orbital $\langle \mathbf{r} | \mathbf{m} \rangle = \phi(\mathbf{r} - \mathbf{m})$ per site. Here $\hat{c}_{\mathbf{m}\sigma}^\dagger$ ($\hat{c}_{\mathbf{m}\sigma}$) is the creation (annihilation) operator of an electron at site $\mathbf{m} = (m_x, m_y)$. The spin-independent hopping matrix element $t_{\mathbf{m}\mathbf{m}'}$ is given by

$$t_{\mathbf{m}\mathbf{m}'} = \left\langle \mathbf{m} \left| -\frac{\hbar^2}{2m^*} \frac{\partial^2}{\partial \mathbf{r}^2} \right| \mathbf{m}' \right\rangle = \begin{cases} -t_O & \text{if } \mathbf{m} = \mathbf{m}' \pm a\mathbf{e}_{x,y} \\ 0 & \text{otherwise.} \end{cases} \quad (29)$$

where $t_O = \hbar^2/(2m^*a^2)$ is the orbital hopping parameter.

6.3.1 Discretization of the Rashba SO Hamiltonian

Following the general discretization procedure outlined above, we recast the Rashba Hamiltonian in the local orbital basis representation as

$$\hat{H} = \sum_{\mathbf{m}\sigma} \varepsilon_{\mathbf{m}} \hat{c}_{\mathbf{m}\sigma}^\dagger \hat{c}_{\mathbf{m}\sigma} + \sum_{\mathbf{m}\mathbf{m}'\sigma\sigma'} \hat{c}_{\mathbf{m}\sigma}^\dagger t_{\mathbf{m}\mathbf{m}'}^{\sigma\sigma'} \hat{c}_{\mathbf{m}'\sigma'}. \quad (30)$$

While this Hamiltonian is of tight-binding type, its hopping parameters are non-trivial 2×2 Hermitian matrices $\mathbf{t}_{\mathbf{m}'\mathbf{m}} = (\mathbf{t}_{\mathbf{m}\mathbf{m}'})^\dagger$ in the spin space. The on-site potential $\varepsilon_{\mathbf{m}}$ describes any static local potential, such as the electrostatic potential due to the applied voltage or the disorder which is usually simulated via a uniform random variable $\varepsilon_{\mathbf{m}} \in [-W/2, W/2]$ modeling short range isotropic scattering off spin-independent impurities. The generalized nearest neighbor hopping $t_{\mathbf{m}\mathbf{m}'}^{\sigma\sigma'} = (\mathbf{t}_{\mathbf{m}\mathbf{m}'})_{\sigma\sigma'}$ accounts for the Rashba coupling

$$\mathbf{t}_{\mathbf{m}\mathbf{m}'} = \begin{cases} -t_O \mathbf{I}_S - it_{\text{SO}} \hat{\sigma}_y & (\mathbf{m} = \mathbf{m}' + \mathbf{e}_x) \\ -t_O \mathbf{I}_S + it_{\text{SO}} \hat{\sigma}_x & (\mathbf{m} = \mathbf{m}' + \mathbf{e}_y) \end{cases}, \quad (31)$$

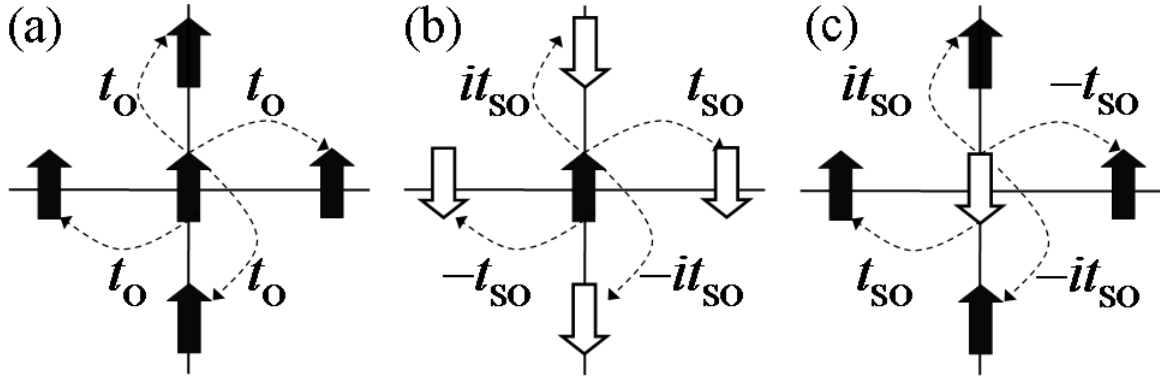


Figure 6: An illustration of the physical meaning of the orbital hopping t_O (a) and the Rashba SO hopping t_{SO} for spin- \uparrow (b) and spin- \downarrow (c) electrons on the tight-binding lattice. As shown in panel (a), the probability amplitude for a spin to hop between two sites without flipping is proportional to t_O . The z -spin $|\uparrow\rangle_z$ at the central site \mathbf{m} in panels (b), (c) flips by jumping to any of the four neighboring sites with probability amplitude proportional to t_{SO} .

through the SO hopping energy scale $t_{SO} = \alpha/2a$ whose physical meaning is illustrated in Fig. 6. It is also useful to express the spin precession length Eq. (20)

$$L_{SO} = \frac{\pi t_O}{2t_{SO}} a, \quad (32)$$

in terms of the lattice spacing a .

A direct correspondence between the continuous effective Rashba Hamiltonian Eq. (14) (with quadratic and isotropic energy-momentum dispersion) and its lattice version Eq. (30) (with tight-binding dispersion) is established by selecting the Fermi energy (e.g., $E_F = -3.8t_O$) of the injected electrons to be close to the bottom of the band $E_b = -4.0t_O$ (so that tight-binding dispersion reduces to the quadratic one), and by using $t_O = \hbar^2/(2m^*a^2)$ for the orbital hopping which yields the effective mass m^* in the continuum limit. For example, the InGaAs/InAlAs heterostructure employed in experiments of Nitta et al. (1997) is characterized by the effective mass $m^* = 0.05m_0$ and the width of the conduction band $\Delta_b = 0.9$ eV, which sets $t_O = \Delta_b/8 = 112$ meV for the orbital hopping parameter on a square lattice (with four nearest neighbors of each site) and $a \simeq 2.6$ nm for its lattice spacing. Thus, the Rashba SO coupling of 2DEG formed in this heterostructure, tuned to a maximum value (Nitta et al., 1997) $\alpha = 0.93 \cdot 10^{-11}$ eVm by the gate electrode, corresponds to the SO hopping $t_{SO}/t_O \simeq 0.016$ in the lattice Hamiltonian Eq. (30).

6.3.2 Discretization of the extrinsic SO Hamiltonian

The extrinsic SO coupling in disordered 2DEG is described by the Pauli Hamiltonian

$$\hat{H} = \frac{\hat{p}_x^2 + \hat{p}_y^2}{2m^*} + V_{\text{conf}}(y) + V_{\text{disorder}}(x, y) + \lambda (\hat{\boldsymbol{\sigma}} \times \hat{\mathbf{p}}) \cdot \nabla V_{\text{disorder}}(x, y), \quad (33)$$

where λ is the extrinsic SO coupling strength. The fourth term in Eq. (33) can be rewritten as

$$\lambda (\hat{\boldsymbol{\sigma}} \times \hat{\mathbf{p}}) \cdot \nabla V_{\text{disorder}}(x, y) = -i\lambda [(\partial_y V_{\text{disorder}}) \partial_x - (\partial_x V_{\text{disorder}}) \partial_y] \hat{\sigma}_z. \quad (34)$$

Equation (23) can then be used to find the discrete version of $\partial_x V_{\text{disorder}}$

$$\begin{aligned} \langle \mathbf{m} | \partial_x V_{\text{disorder}} | \mathbf{m}' \rangle &= \sum_{\mathbf{m}''} \langle \mathbf{m} | \partial_x | \mathbf{m}'' \rangle \langle \mathbf{m}'' | V_{\text{disorder}} | \mathbf{m}' \rangle \\ &= \frac{V_{\text{disorder}}(\mathbf{m} + a\mathbf{e}_x) \delta_{\mathbf{m}', \mathbf{m} + a\mathbf{e}_x} - V_{\text{disorder}}(\mathbf{m} - a\mathbf{e}_x) \delta_{\mathbf{m}', \mathbf{m} - a\mathbf{e}_x}}{2a}. \end{aligned} \quad (35)$$

The final expression (Nikolić and Zârbo, 2007; Dragomirova et. al., 2008) of the discretized version of Eq. (33)

$$\begin{aligned} \hat{H} &= \sum_{\mathbf{m}, \sigma} \varepsilon_{\mathbf{m}} \hat{c}_{\mathbf{m}\sigma}^\dagger \hat{c}_{\mathbf{m}\sigma} - t_0 \sum_{\mathbf{m}\mathbf{m}'\sigma} \hat{c}_{\mathbf{m}\sigma}^\dagger \hat{c}_{\mathbf{m}'\sigma} \\ &\quad - i\lambda_{\text{SO}} \sum_{\mathbf{m}, \alpha\beta} \sum_{ij} \sum_{\nu\gamma} \epsilon_{ijz} \nu\gamma (\varepsilon_{\mathbf{m}+\gamma\mathbf{e}_j} - \varepsilon_{\mathbf{m}+\nu\mathbf{e}_i}) \hat{c}_{\mathbf{m}, \alpha}^\dagger \hat{\sigma}_{\alpha\beta}^z \hat{c}_{\mathbf{m}+\nu\mathbf{e}_i+\gamma\mathbf{e}_j, \beta}, \end{aligned} \quad (36)$$

introduces second neighbor hopping in the third term (in addition to usual nearest neighbor hopping in the second term). Here λ_{SO} is the dimensionless extrinsic SO coupling strength $\lambda_{\text{SO}} = \lambda\hbar/4a^2$ and ϵ_{ijz} stands for the Levi-Civita totally antisymmetric tensor (i, j denote the in-plane coordinate axes and dummy indices ν, γ take values ± 1). For example, for the 2DEG in SHE experiments conducted by Sih et al. (2005), the SO parameters are set to $\lambda_{\text{SO}} \simeq 0.005$ and $t_{\text{SO}} \simeq 0.003t_0$ for an additional Rashba term, assuming conduction bandwidth $\simeq 1$ eV and using the effective mass $m^* = 0.074m_0$.

7 SPIN CURRENT OPERATOR, SPIN DENSITY, AND SPIN ACCUMULATION IN THE PRESENCE OF INTRINSIC SO COUPLINGS

The theory of the intrinsic SHE in infinite homogeneous systems is formulated in terms of the spin current density which is not conserved in media with SO coupling and, therefore, does not have well-defined experimental measurement procedure associated with it. Moreover, these spin current densities can be non-zero even in thermodynamic equilibrium (Rashba, 2003; Nikolić et al., 2006). The conservation of charge implies the continuity equation in quantum mechanics for the charge density $\rho = e|\Psi(\mathbf{r})|^2$

$$\frac{\partial \rho}{\partial t} + \nabla \cdot \mathbf{j} = 0, \quad (37)$$

associated with a given wave function $\Psi(\mathbf{r})$. From here one can extract the charge current density $\mathbf{j} = e\text{Re}[\Psi^\dagger(\mathbf{r})\hat{\mathbf{v}}\Psi(\mathbf{r})]$ viewed as the quantum-mechanical expectation value [in the state $\Psi(\mathbf{r})$] of the charge current density operator

$$\hat{\mathbf{j}} = e \frac{\hat{n}(\mathbf{r})\hat{\mathbf{v}} + \hat{\mathbf{v}}\hat{n}(\mathbf{r})}{2}. \quad (38)$$

This operator can also be obtained heuristically from the classical charge current density $\mathbf{j} = en(\mathbf{r})\mathbf{v}$ via quantization procedure where the particle density $n(\mathbf{r})$ and the velocity \mathbf{v} are

replaced by the corresponding operators and symmetrized to ensure that $\hat{\mathbf{j}}$ is a Hermitian operator.

In SO-coupled systems $\hat{\mathbf{j}}$ acquires extra terms since the velocity operator $i\hbar\hat{\mathbf{v}} = [\hat{\mathbf{r}}, \hat{H}]$ is modified by the presence of SO terms in the Hamiltonian \hat{H} . For example, for the Rashba SO Hamiltonian Eq. (3) the velocity operator is $\hat{\mathbf{v}} = \hat{\mathbf{p}}/m^* - (\alpha/\hbar)(\hat{\sigma}_y\mathbf{e}_x - \hat{\sigma}_x\mathbf{e}_y)$. The spin density $S^i = \frac{\hbar}{2}[\Psi^\dagger(\mathbf{r})\hat{\sigma}_i\Psi(\mathbf{r})]$ then satisfies the following continuity equation

$$\frac{\partial S^i}{\partial t} + \nabla \cdot \mathbf{j}^i = F_S^i. \quad (39)$$

In contrast to the charge continuity equation Eq. (37), this contains the spin current density

$$\mathbf{j}^i = \frac{\hbar}{2}\Psi^\dagger(\mathbf{r})\frac{\hat{\sigma}_i\hat{\mathbf{v}} + \hat{\mathbf{v}}\hat{\sigma}_i}{2}\Psi(\mathbf{r}), \quad (40)$$

as well as a nonzero spin source term

$$F_S^i = \frac{\hbar}{2}\text{Re} \left(\Psi^\dagger(\mathbf{r})\frac{i}{\hbar}[\hat{H}, \hat{\sigma}_i]\Psi(\mathbf{r}) \right). \quad (41)$$

The nonzero $F_S^i \neq 0$ term reflects non-conservation of spin in the presence of intrinsic SO couplings which act as internal momentum-dependent magnetic field forcing spin into precession. Thus, the plausible Hermitian operator of the spin current density

$$\hat{j}_k^i = \frac{\hbar}{2}\frac{\hat{\sigma}_i\hat{v}_k + \hat{v}_k\hat{\sigma}_i}{2}, \quad (42)$$

is a well-defined quantity (a tensor with nine components where \hat{j}_k^i describes transport of spin S_i in the k -direction, $i, k = x, y, z$) only when $\hat{\mathbf{v}}$ is spin independent.

The lack of the usual physical justification for Eq. (42) in systems with intrinsic SO couplings leads to an arbitrariness in the definition of the spin current (Shi et al., 2006). Thus, different definitions lead to ambiguities (Sugimoto et al., 2006) in the value of the intrinsic spin-Hall conductivity $\sigma_{sH} = j_y^z/E_x$ computed as the linear response to the applied longitudinal electric field E_x penetrating an infinite SO-coupled (perfect) crystal. It also yields qualitatively different conclusions about the effect of impurities on SHE (Nagaosa, 2008), and does not allow us to connect (Nomura et al., 2005) directly the value of σ_{sH} to measured edge spin accumulation of opposite signs along opposite lateral edges.

Under the time-reversal transformation, the mass, charge, and energy do not change sign, while the velocity operator and the Pauli matrices change sign, $t \rightarrow -t \Rightarrow \hat{\mathbf{v}} \rightarrow -\hat{\mathbf{v}}$ and $t \rightarrow -t \Rightarrow \hat{\boldsymbol{\sigma}} \rightarrow -\hat{\boldsymbol{\sigma}}$. Since the charge current density operator Eq. (38) contains velocity, it changes sign under the time reversal $t \rightarrow -t \Rightarrow \hat{\mathbf{j}} \rightarrow -\hat{\mathbf{j}}$ and, therefore, has to vanish in the thermodynamic equilibrium [except in the presence of an external magnetic field which breaks time-reversal invariance thereby allowing for circulating or diamagnetic charge currents even in thermodynamic equilibrium (Baranger and Stone, 1989)]. On the other hand, the spin current density operator Eq. (42) is the time-reversal invariant (or even) quantity $t \rightarrow -t \Rightarrow \hat{j}_k^i \rightarrow \hat{j}_k^i$: if the clock ran backward, spin current would continue to flow in the same direction. Thus, \hat{j}_k^i can have non-zero expectation values even in thermodynamic equilibrium. This has been explicitly demonstrated (Rashba, 2003) for the case of an infinite clean

Rashba spin-split 2DEG where such *equilibrium* spin currents are polarized inside the plane. Therefore, the out-of-plane polarized spin current density has been considered as a genuine nonequilibrium SHE-induced response (Sinova et al., 2004; Hankiewicz and Vignale, 2008). However, within multiterminal finite-size Rashba coupled devices even out-of-plane polarized spin currents can have equilibrium nature (Nikolić et al., 2006). This is essential information for the development of a consistent theory for transport (nonequilibrium) spin currents where the contributions from background (equilibrium) currents must be eliminated.

A plausible solution to these issues appears to be in defining a conserved quantity where non-conserved part Eq. (41) is moved to the right-hand side of the continuity equation Eq. (39) and incorporated in the definition of a new spin current operator (Shi et al., 2006). However, this solution is of limited value since it cannot be used for realistic devices with arbitrary boundary conditions due to sample edges and attached electrodes (Nagaosa, 2008). In Sec. 8 we discuss how to bypass these issues altogether by employing NEGF-based description of SHE in realistic finite-size devices where spin transport is quantified through: (i) total spin currents flowing out of the sample through attached leads in which they are conserved due to leads being ideal (i.e., spin and charge interaction free); (ii) local spin currents whose sums in the leads is equal to the total currents of (i); and (iii) nonequilibrium spin density near the boundaries (i.e., edge spin-Hall accumulation that is part of the definition of SHE) or within the SO-coupled sample (which is not typically associated with SHE experimentally measured quantities, but represents natural ingredient of theoretical modeling).

8 NEGF APPROACH TO SPIN TRANSPORT IN MULTITERMINAL SO-COUPLED NANOSTRUCTURES

The NEGF theory (Leeuwen et al., 2006; Rammer, 2007; Haug and Jauho, 2007) provides a powerful conceptual framework, as well as computational tools, to deal with a variety of out-of-equilibrium situations in quantum systems. This includes steady-state transport regime and more general transient responses. Over the past three decades, it has become one of the major tools to study steady-state quantum transport of charge currents through small devices in phase-coherent regime where electron is described by a single wave function throughout the device. In this respect, NEGF offers efficient realization of Landauer's seminal ideas to account for phase-coherent conduction in terms of the scattering matrix of the device (Datta, 1995). Furthermore, NEGF is much more complete framework making it possible to go beyond the paradigms of the Landauer-Büttiker scattering approach by including many-body effects in transport where electron-electron interactions, electronic correlations, and electron-phonon interactions introduce dephasing leading to incoherent electron propagation (Datta, 1995, 2005; Thygesen and Rubio, 2008).

The central concepts in NEGF description of quantum transport are: the sample Hamiltonian \hat{H} and its matrix representation \mathbf{H} in a typically chosen local orbital basis (such as the discrete versions of the effective SO Hamiltonian discussed in Sec. 6.3); the retarded Σ_{leads} and the lesser $\Sigma^<$ self-energy matrices due to the interaction of the sample with the electrodes; self-energy matrices due to many-body interactions within the sample Σ_{int} , $\Sigma^<$; and two independent Green functions—the retarded \mathbf{G} and the lesser $\mathbf{G}^<$ one. The retarded

Green function describes the density of available quantum-mechanical states, while the lesser one determines how electrons occupy those quantum states.⁸

In the case of phase-coherent calculations of total spin and charge currents, we only need to find the retarded spin-resolved self-energies due to the electrodes $\Sigma_{\text{leads}}^\sigma$ (determining the escape rates of spin- σ electrons into the electrodes) and compute the retarded Green function elements connecting sites between interfaces where leads are attached to the sample. For convenience, we term this usage of NEGF “Landauer-Büttiker approach” in Sec. 8.1 since it allows to describe transport in multiterminal structures by constructing the transmission block of the scattering matrix in terms of the (portion of) retarded Green function matrix.

For the computation of local quantities within the sample, we also need to find matrix elements of the retarded Green function between any two sites within the sample as well as $\mathbf{G}^<$. This requires to solve the Keldysh (integral or matrix) equation for $\mathbf{G}^<$. The same is true for incoherent transport where dephasing takes place in the sample requiring Σ_{int} , $\Sigma_{\text{int}}^<$ self-energies to be computed (typically in the self-consistent fashion together with \mathbf{G} and $\mathbf{G}^<$), or for nonlinear transport where local charge density and the corresponding electric potential profile within the sample play a crucial role (Christen and Büttiker, 1996) in understanding the device current-voltage characteristics. We denote this procedure in Sec. 8.2 and Sec. 8.3 as the “Landauer-Keldysh” approach since here the full NEGF theory is applied to finite-size (clean or disordered) devices attached to semi-infinite electrodes, i.e., to the Landauer setup where such electrodes simplify boundary conditions for electrons assumed to escape to infinity through them to be thermalized in the macroscopic reservoirs (ensuring steady-state transport).⁹

8.1 Landauer-Büttiker approach to total spin currents in multiterminal nanostructures

The experiments on quantum Hall bridges in the early 1980s were posing a challenge for theoretical interpretation of multiterminal transport measurements in the mesoscopic transport regime (Ando, 2003). By viewing the current and voltage probes on equal footing, Büttiker (1986) has provided an elegant solution to these puzzles in the form of multiprobe formulas

$$I_p = \sum_q (G_{qp}V_p - G_{pq}V_q) = \sum_q G_{pq}(V_p - V_q). \quad (43)$$

They relate charge current $I_p = I_p^\uparrow + I_p^\downarrow$ in lead p to the voltages V_q in all other leads attached to the sample via the conductance coefficients G_{pq} . To study the spin-resolved charge currents I_p^σ ($\sigma = \uparrow, \downarrow$) of individual spin species \uparrow, \downarrow we imagine that each nonmagnetic lead in Fig. 7

⁸Both Green functions can be obtained from the contour ordered Green function defined for any two time values that lie along Kadanoff-Baym-Keldysh time contour (Leeuwen et al., 2006; Rammer, 2007; Haug and Jauho, 2007).

⁹The NEGF theory, which is often called “Keldysh formalism,” (Leeuwen et al., 2006) has been initiated by the pioneering works of Schwinger, Baym, Kadanoff and Keldysh who considered infinite homogeneous systems out of equilibrium (Rammer, 2007; Haug and Jauho, 2007). Its present applications (Datta, 1995, 2005) to quantum transport in finite-size systems attached to semi-infinite electrodes can be traced to an early analysis of Caroli et al. (1971).

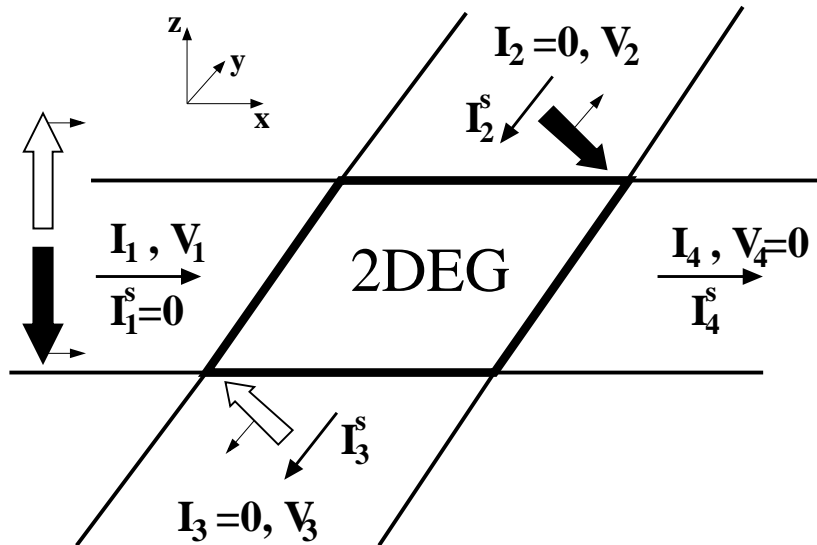


Figure 7: The four-terminal bridge for the detection of the mesoscopic SHE. The central region is 2DEG, where electrons are confined within a semiconductor heterostructure grown along the z -axis whose SIA induces the Rashba SO coupling. The four attached leads are clean, nonmagnetic, and without any SO coupling. The unpolarized ($I_1^S = 0$) charge current ($I_1 \neq 0$) injected through the longitudinal leads induces spin-Hall current $I_2^{S_z} = -I_3^{S_z}$ in the transverse leads which act as the voltage probes $V_2 = V_3 \neq 0$, $I_2 = I_3 = 0$.

consists of the two leads allowing only one spin species to propagate (as realized by, e.g., half-metallic ferromagnetic leads). Upon replacement $I_p \rightarrow I_p^\sigma$ and $G_{pq} \rightarrow G_{pq}^{\sigma\sigma'}$, this viewpoint allows us to extract the multiterminal formulas for the spin-resolved charge currents I_p^σ , thereby obtaining the linear response relation for spin current

$$I_p^S = \frac{\hbar}{2e} (I_p^\uparrow - I_p^\downarrow), \quad (44)$$

flowing through the lead p

$$I_p^S = \frac{\hbar}{2e} \sum_q [(G_{qp}^{\uparrow\uparrow} + G_{qp}^{\downarrow\uparrow} - G_{qp}^{\uparrow\downarrow} - G_{qp}^{\downarrow\downarrow})V_p - (G_{pq}^{\uparrow\uparrow} + G_{pq}^{\uparrow\downarrow} - G_{pq}^{\downarrow\uparrow} - G_{pq}^{\downarrow\downarrow})V_q]. \quad (45)$$

The spin-Hall conductance of the four-terminal bridge sketched in Fig. 7 is then defined as

$$G_{sH} = \frac{\hbar}{2e} \frac{I_2^S}{\Delta V} = \frac{\hbar}{2e} \frac{I_2^\uparrow - I_2^\downarrow}{V_1 - V_4}. \quad (46)$$

Below, we simplify the notation by introducing the labels

$$G_{pq}^{\text{in}} = G_{pq}^{\uparrow\uparrow} + G_{pq}^{\uparrow\downarrow} - G_{pq}^{\downarrow\uparrow} - G_{pq}^{\downarrow\downarrow}, \quad (47a)$$

$$G_{pq}^{\text{out}} = G_{pq}^{\uparrow\uparrow} + G_{pq}^{\downarrow\uparrow} - G_{pq}^{\uparrow\downarrow} - G_{pq}^{\downarrow\downarrow}. \quad (47b)$$

In fact, these coefficients have transparent physical interpretation: $\frac{\hbar}{2e} G_{qp}^{\text{out}} V_p$ is the spin current flowing from the lead p with voltage V_p into other leads q whose voltages are V_q , while $\frac{\hbar}{2e} G_{pq}^{\text{in}} V_q$ is the spin current flowing from the leads $q \neq p$ into the lead p .

The standard charge conductance coefficients (Büttiker, 1986; Baranger and Stone, 1989; Datta, 1995) in the multiprobe Landauer-Büttiker formalism Eq. (43) are expressed in terms of the spin-resolved conductances as $G_{pq} = G_{pq}^{\uparrow\uparrow} + G_{pq}^{\uparrow\downarrow} + G_{pq}^{\downarrow\uparrow} + G_{pq}^{\downarrow\downarrow}$. Their introduction in 1980s was prompted by the need to describe linear transport properties of a single sample (with specific impurity arrangements and attached to specific probe configuration) by using measurable quantities [instead of the bulk conductivity which is inapplicable to mesoscopic conductors (Baranger and Stone, 1989)]. They describe total charge current flowing in and out of the system in response to voltages applied at its boundaries.

Regardless of the detailed microscopic physics of transport, conductance coefficients must satisfy the sum rule $\sum_q G_{qp} = \sum_q G_{pq}$ in order to ensure the second equality in Eq. (43), i.e., the charge current must be zero $V_q = \text{const.} \Rightarrow I_p \equiv 0$ in equilibrium. On the other hand, the multiprobe spin current formulas Eq. (45) apparently possess a nontrivial equilibrium solution $V_q = \text{const.} \Rightarrow I_p^S \neq 0$ [found by Pareek (2004)] that would contradict the Landauer-Büttiker paradigm demanding usage of only measurable quantities. However, when all leads are at the same potential, a purely equilibrium nonzero term, $\frac{\hbar}{2e}(G_{pp}^{\text{out}}V_p - G_{pp}^{\text{in}}V_p) = \frac{\hbar}{e}(G_{pp}^{\downarrow\uparrow} - G_{pp}^{\uparrow\downarrow})V_p$, becomes relevant for I_p^S , canceling all other terms in Eq. (45) to ensure that no *unphysical* total spin current $I_p^S \neq 0$ can appear in the leads of an unbiased ($V_q = \text{const.}$) multiterminal device (Souma and Nikolić, 2005; Kiselev and Kim, 2005; Scheid et al., 2007).

At zero temperature, the spin-resolved conductance coefficients

$$G_{pq}^{\sigma\sigma'} = \frac{e^2}{h} \sum_{ij} |\mathbf{t}_{ij,\sigma\sigma'}^{pq}|^2, \quad (48)$$

where summation is over the conducting channels in the leads, are obtained from the Landauer-type formula as the probability for spin- σ' electron incident in lead q to be transmitted to lead p as spin- σ electron. The quantum-mechanical probability amplitude for this process is given by the matrix elements of the transmission matrix \mathbf{t}^{pq} , which is determined only by the wave functions (or Green functions) at the Fermi energy (Baranger and Stone, 1989). The stationary states of the structure 2DEG + two leads supporting one or two conducting channels can be found exactly by matching the wave functions in the leads to the eigenstates of the Hamiltonian Eq. (14), thereby allowing one to obtain the charge conductance from the Landauer transmission formula (Governale and Zülicke, 2004). However, modeling of the full bridge geometry with two extra leads attached in the transverse direction, the existence of many open transverse propagating modes (“conducting channels”), and possibly strong SO coupling regime when sample is bigger than the spin precession length ($L > L_{\text{SO}}$), is handled much more efficiently through the NEGF formalism.¹⁰

For non-interacting particle which propagates through a finite-size sample of arbitrary shape, the transmission matrices

$$\begin{aligned} \mathbf{t}^{pq} &= \sqrt{-\text{Im} \Sigma_p \otimes \mathbf{I}_S} \cdot \mathbf{G}_{pq} \cdot \sqrt{-\text{Im} \Sigma_q \otimes \mathbf{I}_S}, \\ \text{Im} \Sigma_p &= \frac{1}{2i} (\Sigma_p - \Sigma_p^\dagger), \end{aligned} \quad (49)$$

¹⁰The multiterminal and multichannel finite-size device can be also modeled using the random matrix theory for its scattering matrix (Bardarson et al., 2007). However, this method is strictly applicable only for weak SO coupling regime $L \ll L_{\text{SO}}$ (Aleiner and Fal’ko, 2001).

between different leads can be evaluated in a numerically exact fashion using the real \otimes spin-space retarded Green operator \hat{G}^r defined in the Hilbert space $\mathcal{H}_O \otimes \mathcal{H}_S$. Their matrix representation in a basis $|\mathbf{m}\rangle \otimes |\sigma\rangle \in \mathcal{H}_O \otimes \mathcal{H}_S$ introduced by the Hamiltonian Eq. (30) is obtained through the matrix inversion

$$\mathbf{G} = \frac{1}{E\mathbf{I}_O \otimes \mathbf{I}_S - \mathbf{H} - \sum_{p=1}^4 \Sigma_p \otimes \mathbf{I}_S}, \quad (50)$$

Here $|\sigma\rangle$ are the eigenstates of the spin operator for the chosen spin quantization axis. The matrix elements $\langle \mathbf{m}', \sigma' | \hat{G}^r | \mathbf{m}, \sigma \rangle$ of \mathbf{G} yield the probability amplitude for an electron to propagate between two arbitrary locations \mathbf{m} and \mathbf{m}' (with or without flipping its spin σ during the motion) inside an open conductor in the absence of inelastic processes. Its submatrix \mathbf{G}_{pq} , which is required in Eq. (49), consists of those matrix elements which connects the layer of the sample attached to the lead q to the layer of the sample attached to the lead p . The sum of the self-energy matrices $\sum_{p=1}^4 \Sigma_p \otimes \mathbf{I}_S$ accounts for the ‘‘interaction’’ of an open system with the attached four ideal semi-infinite leads p (Datta, 1995).

8.1.1 General expression for spin-Hall conductance

Since the total charge current $I_p = I_p^\uparrow + I_p^\downarrow$ depends only on the voltage difference between the leads in Fig. 7, we set one of them to zero (e.g., $V_4 = 0$ is chosen as the reference potential) and apply voltage V_1 to the structure. Imposing the requirement $I_2 = I_3 = 0$ for the voltage probes 2 and 3 allows us to get the voltages V_2/V_1 and V_3/V_1 by inverting the multiprobe charge current formulas Eq. (43). Finally, by solving Eq. (45) for I_2^S we obtain the most general expression for the spin-Hall conductance defined by Eq. (46)

$$G_{sH} = \frac{\hbar}{2e} \left[(G_{12}^{\text{out}} + G_{32}^{\text{out}} + G_{42}^{\text{out}}) \frac{V_2}{V_1} - G_{23}^{\text{in}} \frac{V_3}{V_1} - G_{21}^{\text{in}} \right]. \quad (51)$$

This quantity is measured in the units of the spin conductance quantum $e/4\pi$ (as the largest possible G_{sH} when transverse leads support only one open conducting channel), which is the counterpart¹¹ of the familiar charge conductance quantum e^2/h .

In contrast to charge current, which is a scalar quantity, spin current has three components because of the vector nature of spin (i.e., different ‘‘directions’’ of spin correspond to different quantum mechanical superpositions of $|\uparrow\rangle$ and $|\downarrow\rangle$ states). Therefore, we can expect that, in general, the detection of spin transported through the transverse leads of mesoscopic devices will find its expectation values to be nonzero for all three axes. However, their flow properties

$$I_2^{S_z} = -I_3^{S_z}, \quad (52a)$$

$$I_2^{S_x} = -I_3^{S_x}, \quad (52b)$$

$$I_2^{S_y} = I_3^{S_y}, \quad (52c)$$

show that only the z and the x components can represent the SHE response for the Rashba SO-coupled four-terminal bridge. That is, if we connect the transverse leads 2 and 3 to each other

¹¹ Note that $(\hbar/2e)(e^2/h) = e/4\pi$, where (e^2/h) is the natural unit for spin-resolved charge conductance coefficients $G_{pq}^{\sigma\sigma'}$.

(thereby connecting the lateral edges of 2DEG by a wire), only the spin current carrying z - and x -polarized spins will flow through them, as expected from the general SHE phenomenology where nonequilibrium spin-Hall accumulation detected in experiments (Kato et al., 2004a) has opposite sign on the lateral edges of 2DEG.

Therefore, to quantify all nonzero components of the vector of transverse spin current in the linear response regime, we can introduce three spin conductances (Nikolić et al., 2005b)

$$G_{sH}^x = I_2^{S_x}/V_1, \quad (53a)$$

$$G_{sp}^y = I_2^{S_y}/V_1, \quad (53b)$$

$$G_{sH}^z = I_2^{S_z}/V_1, \quad (53c)$$

(assuming $V_4 = 0$). They can be evaluated using the same general formula Eq. (51) where the spin quantization axis for \uparrow, \downarrow in spin-resolved charge conductance coefficients is chosen to be the x, y , or z axis, respectively. For example, selecting $\hat{\sigma}_z|\uparrow\rangle = +|\uparrow\rangle$ and $\hat{\sigma}_z|\downarrow\rangle = -|\downarrow\rangle$ for the basis in which the Green operator Eq. (50) is represented allows one to compute the z -component of the spin current $I_p^{S_z}$. In accord with their origin revealed by Eq. (52), we denote G_{sH}^z and G_{sH}^x as the spin-Hall conductances, while G_{sp}^y is labeled as the ‘‘spin polarization’’ conductance since it stems from the polarization of 2DEG by the flow of unpolarized charge current in the presence of SO couplings (Silsbee, 2004).

8.1.2 Symmetry properties of spin conductances

Symmetry properties of the conductance coefficients with respect to the reversal of a bias voltage or the direction of an external magnetic field play an essential role in our understanding of linear response electron transport in macroscopic and mesoscopic conductors (Büttiker, 1986; Datta, 1995). For example, in the absence of magnetic field they satisfy $G_{pq} = G_{qp}$ [which can be proved assuming a particular model for charge transport (Datta, 1995)]. Moreover, since the effective magnetic field $\mathbf{B}_R(\mathbf{p})$ of the Rashba SO coupling depends on momentum, it does not break the time-reversal invariance thereby imposing the following property of the spin-resolved conductance coefficients $G_{pq}^{\sigma\sigma'} = G_{qp}^{-\sigma'-\sigma}$ in multiterminal SO-coupled bridges.

In addition, the ballistic four-terminal bridge in Fig. 7 with no impurities possesses various geometrical symmetries. It is invariant under rotations and reflections that interchange the leads, such as: (i) rotation C_4 (C_2) by an angle $\pi/2$ (π) around the z axis for a square (rectangular) 2DEG central region; (ii) reflection σ_{vx} in the xz plane; and (iii) reflection σ_{vy} in the yz plane. These geometrical symmetries, together with $G_{pq} = G_{qp}$ property, specify $V_2/V_1 = V_3/V_1 \equiv 0.5$ solution for the voltages of the transverse leads when $I_2 = I_3 = 0$ condition is imposed on their charge currents.

The device Hamiltonian containing the Rashba SO term commutes with the unitary transformations which represent these symmetry operations in the Hilbert space $\mathcal{H}_O \otimes \mathcal{H}_S$: (i) $\hat{U}(C_2) \otimes \exp(i\frac{\pi}{2}\hat{\sigma}_z)$, which performs the transformation $\hat{\sigma}_x \rightarrow -\hat{\sigma}_x$, $\hat{\sigma}_y \rightarrow -\hat{\sigma}_y$, $\hat{\sigma}_z \rightarrow \hat{\sigma}_z$ and interchanges the leads 1 and 4 as well as the leads 2 and 3; (ii) $\hat{U}(\sigma_{vx}) \otimes \exp(i\frac{\pi}{2}\hat{\sigma}_y)$, which transforms the Pauli matrices $\hat{\sigma}_x \rightarrow -\hat{\sigma}_x$, $\hat{\sigma}_y \rightarrow \hat{\sigma}_y$, $\hat{\sigma}_z \rightarrow -\hat{\sigma}_z$ and interchanges leads 2 and 3; and (iii) $\hat{U}(\sigma_{vy}) \otimes \exp(i\frac{\pi}{2}\hat{\sigma}_x)$ which transforms $\hat{\sigma}_x \rightarrow \hat{\sigma}_x$, $\hat{\sigma}_y \rightarrow -\hat{\sigma}_y$, $\hat{\sigma}_z \rightarrow -\hat{\sigma}_z$ and exchanges lead 1 with lead 4. The Hamiltonian also commutes with the time-reversal operator.

The effect of these symmetries on the spin-resolved charge conductance coefficients, and the corresponding spin conductances G_{sH}^z , G_{sH}^x and G_{sp}^y expressed in terms of them through Eq. (51), is as follows. The change in the sign of the spin operator means that spin- \uparrow becomes spin- \downarrow so that, e.g., G_{pq}^{in} will be transformed into $-G_{qp}^{\text{in}}$. Also, the time-reversal implies changing the signs of all spin operators and all momenta so that $G_{pq}^{\sigma\sigma'} = G_{qp}^{-\sigma'-\sigma}$ is equivalent to $G_{pq}^{\text{in}} = -G_{qp}^{\text{out}}$. Thus, invariance with respect to $\hat{U}(\sigma_{vy}) \otimes \exp(i\frac{\pi}{2}\hat{\sigma}_x)$ yields the identities $G_{21}^{\text{in},x} = G_{24}^{\text{in},x}$, $G_{21}^{\text{in},y} = -G_{24}^{\text{in},y}$, and $G_{21}^{\text{in},z} = -G_{24}^{\text{in},z}$. These symmetries do not imply cancellation of $G_{23}^{\text{in},x}$. However, invariance with respect to $\hat{U}(\sigma_{vx}) \otimes \exp(i\frac{\pi}{2}\hat{\sigma}_y)$ and $\hat{U}(C_2) \otimes \exp(i\frac{\pi}{4}\hat{\sigma}_z)$ implies that $G_{23}^{\text{in},y} \equiv 0$ and $G_{23}^{\text{in},z} \equiv 0$.

These symmetry imposed conditions simplify the general formula Eq. (51) for spin conductances of a perfectly clean Rashba SO-coupled four-terminal bridge to

$$G_{sH}^x = \frac{\hbar}{2e} (2G_{12}^{\text{out},x} + G_{32}^{\text{out},x}), \quad (54a)$$

$$G_{sp}^y = \frac{\hbar}{2e} G_{12}^{\text{out},y}, \quad (54b)$$

$$G_{sH}^z = \frac{\hbar}{2e} G_{12}^{\text{out},z}. \quad (54c)$$

where we employ the result $V_2/V_1 = V_3/V_1 \equiv 0.5$ valid for a geometrically symmetric clean bridge. Because this solution for the transverse terminal voltages is violated in disordered bridges, its sample specific (for given impurity configuration) spin conductance cannot be computed from simplified formulas Eq. (54), as it is often assumed in the recent mesoscopic SHE studies (Sheng and Ting, 2006; Ren et al., 2006).

It insightful to apply the same symmetry analysis to the bridges with other types of SO couplings. For example, if the Rashba term in the Hamiltonian Eq. (14) is replaced by the linear Dresselhaus SO term $\frac{\beta}{\hbar}(\hat{p}_x\hat{\sigma}_x - \hat{p}_y\hat{\sigma}_y)$ due to BIA (Žutić et al., 2004), no qualitative change in our analysis ensues since the two SO couplings can be transformed into each other by a unitary matrix $(\hat{\sigma}_x + \hat{\sigma}_y)/\sqrt{2}$. In this case, the spin-Hall response is signified by $I_2^{S_z} = -I_3^{S_z}$ and $I_2^{S_y} = -I_3^{S_y}$ components of the transverse spin current, while $I_2^{S_x} = I_3^{S_x}$. For the Dresselhaus SO-coupled bridge, the general expression Eq. (51) simplifies to

$$G_{sp}^x = \frac{\hbar}{2e} G_{12}^{\text{out},x}, \quad (55a)$$

$$G_{sH}^y = \frac{\hbar}{2e} (2G_{12}^{\text{out},y} + G_{32}^{\text{out},y}), \quad (55b)$$

$$G_{sH}^z = \frac{\hbar}{2e} G_{12}^{\text{out},z}. \quad (55c)$$

The qualitatively different situation emerges when both the Rashba and the linear Dresselhaus SO couplings become relevant in the central region of the bridge since in this case it is impossible to find spin rotation which, combined with the spatial symmetry, would keep the Hamiltonian invariant while only transforming the signs of its spin matrices. Moreover, for such ballistic bridge the condition $I_2 = I_3 = 0$ leads to $V_2/V_1 = 1 - V_3/V_1$ solution for the voltages, whereas imposing the alternative condition $V_2 = V_3$ generates non-zero charge currents flowing through the transverse leads 2 and 3 together with the spin currents [no simple relations akin to Eq. (52) can be written in either of these cases].

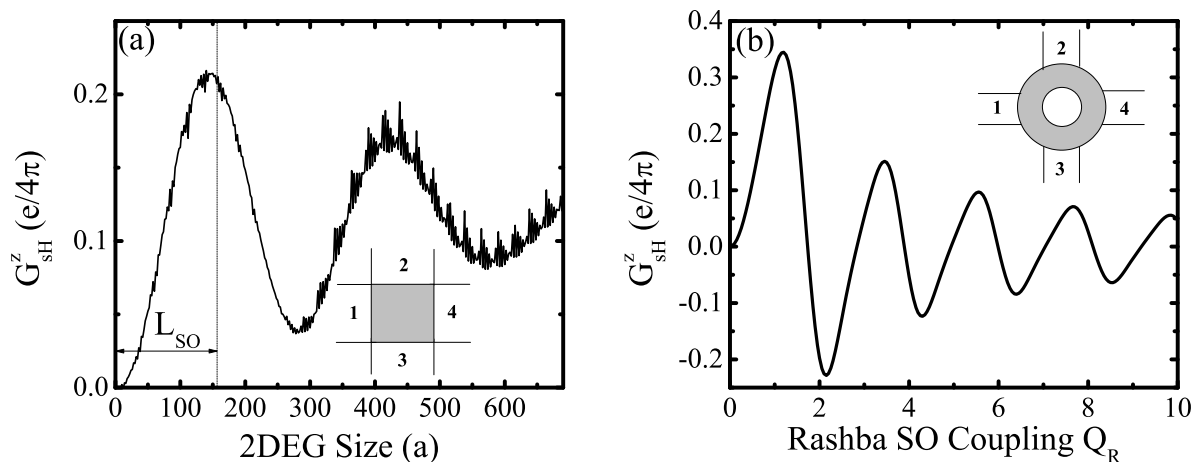


Figure 8: The spin-Hall conductance G_{sH}^z of: (a) Rashba SO-coupled square-shaped 2DEG as the function its size L (in the units of the lattice spacing $a \simeq 3$ nm) for $t_{SO} = 0.01t_O$ setting the spin precession length $L_{SO} \approx 157a$; and (b) single channel Aharonov-Casher ring as the function of the dimensionless Rashba SO coupling $Q_R = (t_{SO}/t_O)N/\pi$ where the number of lattice sites discretizing the ring is $N = 100$.

8.1.3 Example: Transverse total spin currents in mesoscopic and quantum-interference-driven SHE nanostructures

Figure 8 plots two examples of G_{sH}^z computed for simply-connected (square-shaped) 2DEG and multiply-connected ring realized within 2DEG. In both cases, the Rashba SO coupling is present within the device (gray area in the insets of Fig. 8). Figure 8 confirms that optimal device size to observe large mesoscopic SHE in multiterminal structures is indeed governed by L_{SO} (Nikolić et al., 2005b). The computation of SHE conductance for very large square lattices in Fig. 8(a) is made possible by the usage of the recursive Green function algorithm for four-terminal nanostructures discussed in Sec. 9.2.

The spin conductance of the single-channel ring attached to four single-channel ideal leads in Fig. 8(b) illustrates the *quantum-interference driven SHE* introduced by Souma and Nikolić (2005). The ring represent a solid-state realization of the two-slit experiment since an electron entering the ring can propagate in two possible directions—clockwise and counterclockwise. The superpositions of corresponding quantum states are sensitive to the acquired topological phases in a magnetic [Aharonov-Bohm effect] or an electric [Aharonov-Casher effect for particles with spin] external field whose changing generates an oscillatory pattern of the ring conductance. Thus, unlike commonly discussed extrinsic and intrinsic SHE, whose essence can be understood using semiclassical arguments and wave packet propagation (Sinitsyn, 2008), here the Aharonov-Casher phase difference acquired by opposite spin states during their cyclic evolution around the ring plays a crucial role. The spin conductance G_{sH}^z becomes zero at specific values of the Rashba coupling when the destructive interference of opposite spins traveling in opposite directions around the ring takes place (Souma and Nikolić, 2005; Tserkovnyak and Brataas, 2007). The amplitude of such quasiperiodic oscillations of G_{sH}^z , which are absent in simply connected mesoscopic SHE devices of Fig. 8(a), gradually decreases at large Rashba coupling because of the reflection at the ring-lead interface.

8.2 Landauer-Keldysh approach to local spin currents in multiterminal nanostructures

The theory of imaging of charge flow on nanoscale can be constructed efficiently within the framework of lattice models of mesoscopic devices and the corresponding bond charge currents (Baranger and Stone, 1989; Todorov, 2002). This makes it possible to obtain a detailed picture of charge propagation between two arbitrary sites of the lattice (Nonoyama and Oguri, 1998; Cresti et al., 2003; Metalidis and Bruno, 2005; Nikolić et al., 2006; Zârbo and Nikolić, 2007), thereby providing a way to interpret recent scanning probe experiments. These experimental advances (Topinka et al., 2003) have brought new insights into quantum transport by imaging its local features within a single sample, rather than performing conventional measurement of macroscopically averaged quantities. At the same time, scanning probe techniques are becoming increasingly important in the quest for smaller electronic devices. For example, recent imaging of charge flow in conventional $p-n$ junctions suggests that in structures shrunk below 50 nm individual positions of scarce dopants will affect their function, thereby requiring to know precisely how charge carriers propagate on the nanoscale (Yoshida et al., 2007). In the case of spin transport, Kerr rotation microscopy has made possible imaging of steady-state spin density driven by charge flow through various SO-coupled semiconductor structures (Crooker and Smith, 2005; Kato et al., 2005).

In this Section, we discuss NEGF-based tools that allow us to compute the spatial details of spin flow on the scale of few nanometers by introducing the *bond spin currents* (Nikolić et al., 2006). They represent the analog of bond charge currents, as well as a lattice version of the spin current density conventionally employed in the studies of the intrinsic SHE in macroscopic systems (Murakami et al., 2003; Sinova et al., 2004). Even though their sums over the cross sections within the sample change as we move from the bottom to the top transverse electrode due to spin current non-conservation, they illustrate propagation of precessing spins and within the ideal transverse leads their sums over the cross section reproduce (Nikolić et al., 2006) conserved total spin currents discussed in Sec. 8.1 using the Landauer-Büttiker approach.

8.2.1 Bond charge current operator in SO-coupled systems

The charge conservation expressed through the familiar continuity equation Eq. (37) yields a uniquely determined bond charge current operator for quantum systems described on a lattice by a tight-binding-type of Hamiltonian Eq. (30). That is, the Heisenberg equation of motion

$$\frac{d\hat{N}_{\mathbf{m}}}{dt} = \frac{1}{i\hbar} [\hat{N}_{\mathbf{m}}, \hat{H}], \quad (56)$$

for the electron number operator $\hat{N}_{\mathbf{m}}$ on site \mathbf{m} , $\hat{N}_{\mathbf{m}} \equiv \sum_{\sigma=\uparrow,\downarrow} \hat{c}_{\mathbf{m}\sigma}^\dagger \hat{c}_{\mathbf{m}\sigma}$, leads to the charge continuity equation on the lattice

$$e \frac{d\hat{N}_{\mathbf{m}}}{dt} + \sum_{k=x,y} \left(\hat{J}_{\mathbf{m},\mathbf{m}+\mathbf{e}_k} - \hat{J}_{\mathbf{m}-\mathbf{e}_k,\mathbf{m}} \right) = 0. \quad (57)$$

This equation introduces the bond charge-current operator (Todorov, 2002) $\hat{J}_{\mathbf{m}\mathbf{m}'}$, which describes the particle current from site \mathbf{m} to its nearest neighbor site \mathbf{m}' . The ‘bond’ terminology

is supported by a picture where current between two sites is represented by a bundle of flow lines bunched together along a line joining the two sites.

Thus, the spin-dependent Hamiltonian Eq. (30) containing 2×2 hopping matrix defines the bond charge-current operator $\hat{J}_{\mathbf{m}\mathbf{m}'} = \sum_{\sigma\sigma'} \hat{J}_{\mathbf{m}\mathbf{m}'}^{\sigma\sigma'}$ which can be viewed as the sum of four different *spin-resolved* bond charge-current operators

$$\hat{J}_{\mathbf{m}\mathbf{m}'}^{\sigma\sigma'} = \frac{e}{i\hbar} \left[\hat{c}_{\mathbf{m}'\sigma'}^\dagger t_{\mathbf{m}'\mathbf{m}}^{\sigma'\sigma} \hat{c}_{\mathbf{m}\sigma} - \text{H.c.} \right], \quad (58)$$

where H.c. stands for the Hermitian conjugate of the first term. In particular, for the case of $t_{\mathbf{m}\mathbf{m}'}^{\sigma\sigma'}$ being determined by the Rashba SO interaction Eq. (31), we can decompose the bond charge current operator into two terms, $\hat{J}_{\mathbf{m}\mathbf{m}'} = \hat{J}_{\mathbf{m}\mathbf{m}'}^{\text{kin}} + \hat{J}_{\mathbf{m}\mathbf{m}'}^{\text{SO}}$, having transparent physical interpretation. The first term

$$\hat{J}_{\mathbf{m}\mathbf{m}'}^{\text{kin}} = \frac{eit_{\text{O}}}{\hbar} \sum_{\sigma} \left[\hat{c}_{\mathbf{m}'\sigma}^\dagger \hat{c}_{\mathbf{m}\sigma} - \text{H.c.} \right], \quad (59)$$

can be denoted as “kinetic” since it originates only from the kinetic energy t_{O} and does not depend on the SO coupling energy t_{SO} . On the other hand, the second term

$$\begin{aligned} \hat{J}_{\mathbf{m}\mathbf{m}'}^{\text{SO}} &= \begin{cases} -\frac{4et_{\text{SO}}}{\hbar^2} \hat{S}_{\mathbf{m}\mathbf{m}'}^y & (\mathbf{m} = \mathbf{m}' + \mathbf{e}_x) \\ +\frac{4et_{\text{SO}}}{\hbar^2} \hat{S}_{\mathbf{m}\mathbf{m}'}^x & (\mathbf{m} = \mathbf{m}' + \mathbf{e}_y) \end{cases} \\ &= \frac{4et_{\text{SO}}}{\hbar^2} \left((\mathbf{m}' - \mathbf{m}) \times \hat{\mathbf{S}}_{\mathbf{m}\mathbf{m}'} \right)_z \end{aligned} \quad (60)$$

represents additional contribution to the intersite charge current flow due to non-zero Rashba SO hopping t_{SO} . Here we also introduce the “bond spin-density” operator

$$\hat{\mathbf{S}}_{\mathbf{m}\mathbf{m}'} = \frac{\hbar}{4} \sum_{\alpha\beta} \left[\hat{c}_{\mathbf{m}'\alpha}^\dagger \hat{\boldsymbol{\sigma}}_{\alpha\beta} \hat{c}_{\mathbf{m}\beta} + \text{H.c.} \right], \quad (61)$$

defined for the bond connecting the sites \mathbf{m} and \mathbf{m}' , which reduces to the usual definition of the local spin density operator for $\mathbf{m} = \mathbf{m}'$ [see Eq. (74)].

8.2.2 Nonequilibrium bond charge current in SO-coupled systems

The formalism of bond charge current makes it possible to compute physically measurable (Topinka et al., 2003) spatial profiles of local charge current density within the sample as the quantum-statistical average¹² of the bond charge-current operator in the nonequilibrium state (Caroli et al., 1971; Nonoyama and Oguri, 1998; Cresti et al., 2003),

$$\langle \hat{J}_{\mathbf{m}\mathbf{m}'} \rangle = \sum_{\sigma\sigma'} \langle \hat{J}_{\mathbf{m}\mathbf{m}'}^{\sigma\sigma'} \rangle, \quad (62)$$

$$\langle \hat{J}_{\mathbf{m}\mathbf{m}'}^{\sigma\sigma'} \rangle = \frac{-e}{\hbar} \int_{-\infty}^{\infty} \frac{dE}{2\pi} \left[t_{\mathbf{m}'\mathbf{m}}^{\sigma'\sigma} G_{\mathbf{m}\mathbf{m}',\sigma\sigma'}^<(E) - t_{\mathbf{m}\mathbf{m}'}^{\sigma\sigma'} G_{\mathbf{m}'\mathbf{m},\sigma'\sigma}^<(E) \right]. \quad (63)$$

¹² The quantum statistical average $\langle \hat{A} \rangle = \text{Tr}[\hat{\rho}\hat{A}]$ is taken with respect to the density matrix $\hat{\rho}$ that has evolved over sufficiently long time, so that nonequilibrium state and all relevant interactions are fully established.

Here the local charge current is expressed in terms of the nonequilibrium lesser Green function $G_{\mathbf{m}'\mathbf{m},\sigma\sigma'}^<(E)$.

The usage of the second quantized notation in Eq. (30) facilitates the introduction of NEGF expressions for the nonequilibrium expectation values (Caroli et al., 1971; Nonoyama and Oguri, 1998). We imagine that at time $t' = -\infty$ the sample and the leads are not connected, while the left and the right longitudinal lead of a four-probe device are in their own thermal equilibrium with the chemical potentials μ_L and μ_R , respectively, where $\mu_L = \mu_R + eV$. The adiabatic switching of the hopping parameter connecting the leads and the sample generates time evolution of the density matrix of the structure (Caroli et al., 1971). The physical quantities are obtained as the nonequilibrium statistical average $\langle \dots \rangle$ [with respect to the density matrix (Keldysh, 1965) at time $t' = 0$] of the corresponding quantum-mechanical operators expressed in terms of $\hat{c}_{\mathbf{m}\sigma}^\dagger$ and $\hat{c}_{\mathbf{m}\sigma}$. This will lead to the expressions of the type $\langle \hat{c}_{\mathbf{m}\sigma}^\dagger \hat{c}_{\mathbf{m}'\sigma'} \rangle$, which define the lesser Green function (Caroli et al., 1971; Nonoyama and Oguri, 1998)

$$\langle \hat{c}_{\mathbf{m}\sigma}^\dagger \hat{c}_{\mathbf{m}'\sigma'} \rangle = \frac{\hbar}{i} G_{\mathbf{m}'\mathbf{m},\sigma\sigma'}^<(\tau = 0) = \frac{1}{2\pi i} \int_{-\infty}^{\infty} dE G_{\mathbf{m}'\mathbf{m},\sigma\sigma'}^<(E). \quad (64)$$

Here we utilize the fact that the two-time correlation function $[\hat{c}_{\mathbf{m}\sigma}(t) = e^{i\hat{H}t/\hbar} \hat{c}_{\mathbf{m}\sigma} e^{-i\hat{H}t/\hbar}]$

$$G_{\mathbf{m}\mathbf{m}',\sigma\sigma'}^<(t, t') \equiv \frac{i}{\hbar} \langle \hat{c}_{\mathbf{m}'\sigma'}^\dagger(t') \hat{c}_{\mathbf{m}\sigma}(t) \rangle, \quad (65)$$

depends only on $\tau = t - t'$ in stationary situations, so the time difference τ can be Fourier transformed to energy

$$G_{\mathbf{m}\mathbf{m}',\sigma\sigma'}^<(\tau) = \frac{1}{2\pi\hbar} \int_{-\infty}^{\infty} dE G_{\mathbf{m}\mathbf{m}',\sigma\sigma'}^<(E) e^{iE\tau/\hbar}, \quad (66)$$

which will be utilized for steady-state transport studied here. We use the notation where $\mathbf{G}_{\mathbf{m}\mathbf{m}'}^<$ is a 2×2 matrix in the spin space whose $\sigma\sigma'$ element is $G_{\mathbf{m}\mathbf{m}',\sigma\sigma'}^<$.

The spin-resolved bond charge current in Eq. (63) describes the flow of charges which start as spin σ electrons at the site \mathbf{m} and end up as a spin σ' electrons at the site \mathbf{m}' where possible spin-flips $\sigma \neq \sigma'$ (instantaneous or due to precession) are caused by spin-dependent interactions. The decomposition of the bond charge-current operator into the kinetic and SO terms leads to a Green function expression for the corresponding nonequilibrium bond charge currents

$$\langle \hat{J}_{\mathbf{m}\mathbf{m}'} \rangle = \langle \hat{J}_{\mathbf{m}\mathbf{m}'}^{\text{kin}} \rangle + \langle \hat{J}_{\mathbf{m}\mathbf{m}'}^{\text{SO}} \rangle, \quad (67)$$

with kinetic and SO terms given by

$$\langle \hat{J}_{\mathbf{m}\mathbf{m}'}^{\text{kin}} \rangle = \frac{et_0}{\hbar} \int_{-\infty}^{\infty} \frac{dE}{2\pi} \text{Tr}_S [\mathbf{G}_{\mathbf{m}\mathbf{m}'}^<(E) - \mathbf{G}_{\mathbf{m}'\mathbf{m}}^<(E)], \quad (68)$$

$$\langle \hat{J}_{\mathbf{m}\mathbf{m}'}^{\text{SO}} \rangle = \frac{et_{\text{SO}}}{\hbar} \int_{-\infty}^{\infty} \frac{dE}{2\pi i} \text{Tr}_S \{ [(\mathbf{m}' - \mathbf{m}) \times \hat{\boldsymbol{\sigma}}]_z [\mathbf{G}_{\mathbf{m}\mathbf{m}'}^<(E) + \mathbf{G}_{\mathbf{m}'\mathbf{m}}^<(E)] \}. \quad (69)$$

Note, however, that “kinetic” term is also influenced by the SO coupling through $\mathbf{G}^<$. In the absence of the SO coupling, Eq. (69) vanishes and the bond charge current reduces to

the standard expression (Caroli et al., 1971; Nonoyama and Oguri, 1998; Cresti et al., 2003). The trace Tr_S is performed in the spin Hilbert space. Similarly, we can also obtain the nonequilibrium local charge density in terms of $\mathbf{G}^<$

$$\begin{aligned} e \langle \hat{N}_{\mathbf{m}} \rangle &= e \sum_{\sigma=\uparrow,\downarrow} \langle \hat{c}_{\mathbf{m}\sigma}^\dagger \hat{c}_{\mathbf{m}\sigma} \rangle = \frac{e}{2\pi i} \int_{-\infty}^{\infty} dE \sum_{\sigma} G_{\mathbf{m}\mathbf{m},\sigma\sigma}^<(E) \\ &= \frac{e}{2\pi i} \int_{-\infty}^{\infty} dE \text{Tr}_S[\mathbf{G}_{\mathbf{m}\mathbf{m}}^<(E)], \end{aligned} \quad (70)$$

which is the statistical average value of the corresponding operator.

8.2.3 Bond spin current operator in SO-coupled systems

To mimic the plausible definition of the spin-current density operator j_k^i in Eq. (42), we introduce the bond spin-current operator for the spin- S_i component as the symmetrized product of the spin- $\frac{1}{2}$ operator $\hbar\hat{\sigma}_i/2$ ($i = x, y, z$) and the bond charge-current operator from Eq. (57)

$$\hat{j}_{\mathbf{m}\mathbf{m}'}^{S_i} \equiv \frac{1}{4i} \sum_{\alpha\beta} \left[\hat{c}_{\mathbf{m}'\beta}^\dagger \{ \hat{\sigma}_i, \mathbf{t}_{\mathbf{m}'\mathbf{m}} \}_{\beta\alpha} \hat{c}_{\mathbf{m}\alpha} - \text{H.c.} \right]. \quad (71)$$

By inserting the hopping matrix $\mathbf{t}_{\mathbf{m}'\mathbf{m}}$ Eq. (31) of the lattice SO Hamiltonian into this expression we obtain its explicit form for the case of the Rashba coupled system

$$\hat{j}_{\mathbf{m}\mathbf{m}'}^{S_i} = \frac{it_0}{2} \sum_{\alpha\beta} \left(\hat{c}_{\mathbf{m}'\beta}^\dagger (\hat{\sigma}_i)_{\beta\alpha} \hat{c}_{\mathbf{m}\alpha} - \text{H.c.} \right) + t_{\text{SO}} \hat{N}_{\mathbf{m}\mathbf{m}'} [\mathbf{e}_i \times (\mathbf{m}' - \mathbf{m})]_z, \quad (72)$$

which can be considered as the lattice version of Eq. (42). Here we simplify the notation by using the ‘‘bond electron-number operator’’ $\hat{N}_{\mathbf{m}\mathbf{m}'} \equiv \frac{1}{2} \sum_{\sigma} \left(\hat{c}_{\mathbf{m}'\sigma}^\dagger \hat{c}_{\mathbf{m}\sigma} + \text{H.c.} \right)$, which reduces to the standard electron-number operator for $\mathbf{m} = \mathbf{m}'$.

8.2.4 Nonequilibrium bond spin currents in SO-coupled systems

Similarly to the case of the nonequilibrium bond charge current in Sec. 8.2.2, the nonequilibrium statistical average of the bond spin-current operator Eq. (72) can be expressed using the lesser Green function $\mathbf{G}^<$ as

$$\langle \hat{j}_{\mathbf{m}\mathbf{m}'}^{S_i} \rangle = \langle \hat{j}_{\mathbf{m}\mathbf{m}'}^{S_i(\text{kin})} \rangle + \langle \hat{j}_{\mathbf{m}\mathbf{m}'}^{S_i(\text{so})} \rangle, \quad (73a)$$

$$\langle \hat{j}_{\mathbf{m}\mathbf{m}'}^{S_i(\text{kin})} \rangle = \frac{t_0}{2} \int_{-\infty}^{\infty} \frac{dE}{2\pi} \text{Tr}_S [\hat{\sigma}_i (\mathbf{G}_{\mathbf{m}'\mathbf{m}}^<(E) - \mathbf{G}_{\mathbf{m}\mathbf{m}'}^<(E))], \quad (73b)$$

$$\langle \hat{j}_{\mathbf{m}\mathbf{m}'}^{S_i(\text{so})} \rangle = [\mathbf{e}_i \times (\mathbf{m}' - \mathbf{m})]_z \frac{t_{\text{SO}}}{2} \int_{-\infty}^{\infty} \frac{dE}{2\pi i} \text{Tr}_S [\mathbf{G}_{\mathbf{m}\mathbf{m}'}^<(E) + \mathbf{G}_{\mathbf{m}'\mathbf{m}}^<(E)]. \quad (73c)$$

Here we also encounter two terms which can be interpreted as the kinetic and the SO contribution to the bond spin current crossing from site \mathbf{m} to site \mathbf{m}' . However, we emphasize that such SO contribution to the spin- S_z bond current is identically equal to zero, which simplifies the expression for this component to Eq. (73b) as the primary spin current response in the SHE.

8.3 Landauer-Keldysh approach to local spin densities

Motivated by recent advances in Kerr rotation microscopy, which have made possible experimental imaging of steady-state spin polarization in various SO-coupled semiconductor structures (Crooker and Smith, 2005; Kato et al., 2005), we discuss in this Section a NEGF-based approach to computation of the spatial profiles of $\langle \hat{\mathbf{S}}_{\mathbf{m}} \rangle$. Unlike local spin current density, such *local flowing spin density* is a well-defined and measurable quantity that offers insight into the spin flow in the nonequilibrium steady transport state. For $\langle \hat{\mathbf{S}}_{\mathbf{m}} \rangle$ computed at the lateral edges of the sample, we use the term “spin accumulation” which was directly measured in the seminal spin-Hall experiments (Kato et al., 2004a; Wunderlich et al., 2005).

8.3.1 Local spin density and its continuity equation

The local spin density in the lattice models is determined by the local spin operator $\hat{\mathbf{S}}_{\mathbf{m}} = (\hat{S}_{\mathbf{m}}^x, \hat{S}_{\mathbf{m}}^y, \hat{S}_{\mathbf{m}}^z)$ at site \mathbf{m} defined by

$$\hat{\mathbf{S}}_{\mathbf{m}} = \frac{\hbar}{2} \sum_{\alpha\beta} \hat{c}_{\mathbf{m}\alpha}^\dagger \hat{\boldsymbol{\sigma}}_{\alpha\beta} \hat{c}_{\mathbf{m}\beta}. \quad (74)$$

The Heisenberg equation of motion for each component $\hat{\mathbf{S}}^i$ ($i = x, y, z$) of the spin density operator

$$\frac{d\hat{S}_{\mathbf{m}}^i}{dt} = \frac{1}{i\hbar} [\hat{S}_{\mathbf{m}}^i, \hat{H}], \quad (75)$$

can be written in the form

$$\frac{d\hat{S}_{\mathbf{m}}^i}{dt} + \sum_{k=x,y} \left(\hat{J}_{\mathbf{m},\mathbf{m}+\mathbf{e}_k}^{S_i} - \hat{J}_{\mathbf{m}-\mathbf{e}_k,\mathbf{m}}^{S_i} \right) = \hat{F}_{\mathbf{m}}^{S_i}, \quad (76)$$

where $\hat{J}_{\mathbf{m}\mathbf{m}'}^{S_i}$ is the bond spin-current operator given by Eq. (71) so that the second term on the left-hand side of Eq. (76) corresponds to the “divergence” of the bond spin current on site \mathbf{m} . Here, in analogy with Eq. (41), we also find the lattice version of the spin source operator $\hat{F}_{\mathbf{m}}^{S_i}$ whose explicit form is

$$\hat{F}_{\mathbf{m}}^{S_x} = -\frac{t_{\text{SO}}}{t_0} \left(\hat{J}_{\mathbf{m},\mathbf{m}+\mathbf{e}_x}^{S_z} + \hat{J}_{\mathbf{m}-\mathbf{e}_x,\mathbf{m}}^{S_z} \right), \quad (77a)$$

$$\hat{F}_{\mathbf{m}}^{S_y} = -\frac{t_{\text{SO}}}{t_0} \left(\hat{J}_{\mathbf{m},\mathbf{m}+\mathbf{e}_y}^{S_z} + \hat{J}_{\mathbf{m}-\mathbf{e}_y,\mathbf{m}}^{S_z} \right), \quad (77b)$$

$$\hat{F}_{\mathbf{m}}^{S_z} = \frac{t_{\text{SO}}}{t_0} \left(\hat{J}_{\mathbf{m},\mathbf{m}+\mathbf{e}_x}^{S_x} + \hat{J}_{\mathbf{m}-\mathbf{e}_x,\mathbf{m}}^{S_x} + \hat{J}_{\mathbf{m},\mathbf{m}+\mathbf{e}_y}^{S_y} + \hat{J}_{\mathbf{m}-\mathbf{e}_y,\mathbf{m}}^{S_y} \right). \quad (77c)$$

The presence of the non-zero term $\hat{F}_{\mathbf{m}}^{S_i}$ on the right-hand side of the spin continuity Eq. (76) signifies, within the framework of bond spin currents, the fact that spin is not conserved in SO-coupled systems. The fact that the bond spin current operator Eq. (71) appears in the spin continuity equation Eq. (76) as its divergence implies that its definition in Eq. (71) is plausible. However, the presence of the spin source operator $\hat{F}_{\mathbf{m}}^{S_i}$ reminds us that such

definition cannot be made unique (Shi et al., 2006), in sharp contrast to bond charge current which is uniquely determined by the charge continuity Eq. (57).

Evaluating the statistical average of Eq. (76) in a steady state (which can be either equilibrium or nonequilibrium), leads to the identity

$$\sum_{k=x,y} \left(\langle \hat{J}_{\mathbf{m},\mathbf{m}+\mathbf{e}_k}^{S_i} \rangle - \langle \hat{J}_{\mathbf{m}-\mathbf{e}_k,\mathbf{m}}^{S_i} \rangle \right) = \langle \hat{F}_{\mathbf{m}}^{S_i} \rangle. \quad (78)$$

In particular, for the spin- S_z component we get

$$\sum_{k=x,y} \left(\langle \hat{J}_{\mathbf{m},\mathbf{m}+\mathbf{e}_k}^{S_z} \rangle - \langle \hat{J}_{\mathbf{m}-\mathbf{e}_k,\mathbf{m}}^{S_z} \rangle \right) = \frac{t_{\text{SO}}}{t_0} \sum_{k=x,y} \left(\langle \hat{J}_{\mathbf{m},\mathbf{m}+\mathbf{e}_k}^{S_x} \rangle + \langle \hat{J}_{\mathbf{m}-\mathbf{e}_k,\mathbf{m}}^{S_y} \rangle \right), \quad (79)$$

which relates the divergence of the spin- S_z current (left-hand side) to the spin-source (right-hand side) determined by the sum of the longitudinal component of the spin- S_x current and the transverse component of the spin- S_y current.

Since no experiment has been proposed to measure local spin current density within the SO coupled sample, defined through Eq. (40) or its lattice equivalent Eq. (73), we can obtain additional information about the spin fluxes within the sample by computing

$$\begin{aligned} \langle \hat{\mathbf{S}}_{\mathbf{m}} \rangle &= \frac{\hbar}{2} \sum_{\alpha,\beta=\uparrow,\downarrow} \hat{\sigma}_{\alpha\beta} \langle \hat{c}_{\mathbf{m}\alpha}^\dagger \hat{c}_{\mathbf{m}\beta} \rangle = \frac{\hbar}{4\pi i} \int_{-\infty}^{\infty} dE \sum_{\alpha,\beta=\uparrow,\downarrow} \hat{\sigma}_{\alpha\beta} G_{\mathbf{m}\mathbf{m},\beta\alpha}^<(E) \\ &= \frac{\hbar}{4\pi i} \int_{-\infty}^{\infty} dE \text{Tr}_s [\hat{\sigma} \mathbf{G}_{\mathbf{m}\mathbf{m}}^<(E)], \end{aligned} \quad (80)$$

as the nonequilibrium spin density driven by charge transport in the presence of SO couplings.

8.4 Spin-resolved NEGFs for finite-size multiterminal devices

The spin-dependent NEGF formalism discussed in Sec. 8.2 does not actually depend on the details of the external driving force which brings the system into a nonequilibrium state. That is, the system can be driven by either the homogeneous electric field applied to an infinite homogeneous 2DEG or the voltage (i.e., electrochemical potential) difference between the electrodes attached to a *finite-size* sample. For example, in the latter case, the external bias voltage only shifts the relative chemical potentials of the reservoirs into which the longitudinal leads (employed to simplify the boundary conditions) eventually terminate, so that the electrons do not feel any electric field in the course of ballistic propagation through clean 2DEG central region. The information about these different situations is encoded into the lesser Green function $\mathbf{G}^<$.

Here we focus on experimentally relevant spin-Hall devices where finite-size central region (C), defined on the $L \times L$ lattice, is attached to four external semi-infinite leads of the same width L . The leads at infinity terminate into the reservoirs where electrons are brought into thermal equilibrium, characterized by the Fermi-Dirac distribution function $f(E - eV_p)$, to ensure the steady-state transport. In such multiterminal Landauer setup (Büttiker, 1986; Baranger and Stone, 1989; Datta, 1995), current is limited by quantum transmission through a potential profile while power is dissipated non-locally in the reservoirs. The voltage in each

lead of the four-terminal spin-Hall bridge is V_p ($p = 1, \dots, 4$), so that the on-site potential $\varepsilon_{\mathbf{m}}$ within the leads has to be shifted by eV_p .

The spin-dependent lesser Green function $\mathbf{G}^<$ defined in Eq. (65) is evaluated within the finite-size sample region as a $2L^2 \times 2L^2$ matrix in the site \otimes spin space through the spin-resolved matrix Keldysh equation (Keldysh, 1965)

$$\mathbf{G}^<(E) = \mathbf{G}(E)\Sigma^<(E)\mathbf{G}^\dagger(E), \quad (81)$$

which is valid for steady-state transport (i.e., when transients have died away). Within the effective single-particle picture, the retarded Green function is computed by inverting the Hamiltonian of an open system sample+leads

$$\mathbf{G}(E) = \left[E\mathbf{I}_C - \mathbf{H}_C - eU_{\mathbf{m}} - \sum_p \Sigma_p(E - eV_p) \right]^{-1}. \quad (82)$$

Here the retarded $\Sigma_p(E)$ and the lesser $\Sigma^<(E)$ self-energy matrices

$$\Sigma_p(E) = \mathbf{H}_{pC}^\dagger [(E + i0_+) \mathbf{I}_p - \mathbf{H}_p^{\text{lead}}]^{-1} \mathbf{H}_{pC}, \quad (83)$$

$$\Gamma_p(E) = i [\Sigma_p(E) - \Sigma_p^\dagger(E)], \quad (84)$$

$$\Sigma^<(E) = i \sum_p \Gamma_p(E - eV_p) f(E - eV_p), \quad (85)$$

are exactly computable in the non-interacting electron approximation and without any inelastic processes taking place within the sample. They account for the ‘‘interaction’’ of the SO-coupled sample with the attached leads, thereby generating a finite lifetime that electron spends within the 2DEG before escaping through the leads toward the macroscopic thermalizing reservoirs. Here \mathbf{I}_C is the $2L^2 \times 2L^2$ identity matrix and \mathbf{I}_p is the identity matrix in the infinite site \otimes spin space of the lead p . We use the following Hamiltonian matrices

$$(\mathbf{H}_C)_{\mathbf{m}\mathbf{m}',\sigma\sigma'} = \langle 1_{\mathbf{m}\sigma} | \hat{H} | 1_{\mathbf{m}'\sigma'} \rangle, \quad (\mathbf{m}, \mathbf{m}' \in C), \quad (86a)$$

$$(\mathbf{H}_p^{\text{lead}})_{\mathbf{m}\mathbf{m}',\sigma\sigma'} = \langle 1_{\mathbf{m}\sigma} | \hat{H} | 1_{\mathbf{m}'\sigma'} \rangle, \quad (\mathbf{m}, \mathbf{m}' \in p), \quad (86b)$$

$$(\mathbf{H}_{pC})_{\mathbf{m}\mathbf{m}',\sigma\sigma'} = \langle 1_{\mathbf{m}\sigma} | \hat{H} | 1_{\mathbf{m}'\sigma'} \rangle, \quad (\mathbf{m} \in p, \mathbf{m}' \in C), \quad (86c)$$

where $|1_{\mathbf{m}\sigma}\rangle$ is a vector in the Fock space (meaning that the occupation number is one for the single particle state $|\mathbf{m}\sigma\rangle$ and zero otherwise) and \hat{H} is the Hamiltonian given in Eq. (30).

In the general case of arbitrary applied bias voltage, the gauge invariance of measurable quantities (such as the current-voltage characteristics) with respect to the shift of electric potential everywhere by a constant V_c , $eV_p \rightarrow eV_p + eV_c$ and $eU_{\mathbf{m}} \rightarrow eU_{\mathbf{m}} + eV_c$, is satisfied on the proviso that the retarded self-energies $\Sigma_p(E - eV_p)$ introduced by each lead depend explicitly on the applied voltages at the sample boundary, while the computation of the retarded Green function $\mathbf{G}(E)$ has to include the electric potential landscape¹³ $U_{\mathbf{m}}$ within the sample (Christen and Büttiker, 1996). However, when the applied bias is low, so that linear response zero-temperature quantum transport takes place through the sample [as determined by $\mathbf{G}(E_F)$], the exact profile of the internal potential becomes irrelevant (Baranger and Stone, 1989; Nikolić and Allen, 1999).

¹³ The potential landscape $U_{\mathbf{m}}$ can be obtained from the Poisson equation with charge density Eq. (70) as the source.

8.4.1 How to introduce dephasing into SHE nanostructures

Much of the applications of NEGF techniques to mesoscopic semiconductor and nanoscopic molecular systems treat phase-coherent transport by relying on some type of the Landauer transmission formula (Rocha et al., 2006). On the other hand, applications demand devices operating at room temperature where device size is typically much bigger than the dephasing length so that one seldom observes quantum interference effects in the transmission due to multiple scattering off impurities and boundaries. Since such quantum coherence effects are also seen in the linear response spin density in SO-coupled quantum wires, typically computed at zero-temperature (Nikolić et al., 2005c; Reynoso et al., 2006), to compare such calculations with experiments conducted at finite temperature it is desirable to introduce dephasing into NEGF formalism in a simple yet controllable fashion (which leaves the charge current conservation intact).

The most widely used example of the simple approach to inclusion of dephasing are fictitious Büttiker voltage probes (Büttiker, 1986), such as one-dimensional electrodes attached at each site \mathbf{m} of the lattice and with their electrochemical potential adjusted to ensure that the current drawn by each probe is zero.¹⁴ In NEGF formalism this introduces additional self-energy whose matrix elements are $(\Sigma_{\text{deph}})_{\mathbf{m}\mathbf{m},\sigma\sigma} = -i\eta$ for all sites \mathbf{m} within the sample except for those where the external electrodes are attached (Golizadeh-Mojarad and Datta, 2007a). However, while Büttiker probes coupled to each site can remove sharp features in the transmission of the device, they also introduce additional scattering events thereby artificially enhancing the resistance.

A “momentum conserving” phenomenological model for dephasing, that is easily implemented within the NEGF formalism, has recently been proposed by Golizadeh-Mojarad and Datta (2007a). Here the self-energies are taken as $\Sigma_{\text{deph}}(E) = d_i \mathbf{G}(E)$ and $\Sigma_{\text{deph}}^<(E) = d_i \mathbf{G}^<(E)$, with parameter d_i controlling the strength of the elastic dephasing processes. This choice is motivated by the general expressions for the first-order self-consistent Born approximation for the self-energies which ensure the current conservation (Leeuwen et al., 2006). The additional choice of the function multiplying matrix elements of NEGFs is taken to guarantee momentum conservation, so that dephasing does not artifactually enhance the resistance (Golizadeh-Mojarad and Datta, 2007a). This form of the retarded and lesser self-energies requires that Eq. (82) be solved self-consistently [with the initial guess for $\mathbf{G}(E)$ being the solution with no dephasing] and then use such $\mathbf{G}(E)$ to solve the Keldysh equation Eq. (81) directly as the Sylvester equation of matrix algebra. This allows one to compare NEGF calculations (Golizadeh-Mojarad and Datta, 2007b) to SHE experiments all the way to room temperature. Another simple way to smear sharp features in the local spin density due to quantum coherence is averaging over an energy interval (Nikolić et al., 2005c), as shown in Fig. 9. For more details about different NEGF-based simple models of dephasing in quantum transport and their effect on momentum and spin relaxation see the chapter 3 by R. Golizadeh-Mojarad and S. Datta in this Volume.

¹⁴Since current through Büttiker probes is fixed to be zero, then for every electron that enters the lead and is absorbed by the corresponding reservoir another one will come with phase memory washed out due to equilibration by inelastic effects assumed to take place in the reservoir. Thus, this method introduces inelastic effects in a simple phenomenological way.

8.5 Example: Local spin density and spin currents in mesoscopic SHE nanostructures

Figure 9(a) shows NEGF computation (Nikolić et al., 2005c) of spin density within the Rashba coupled 2DEG where all essential features of the experimentally observed SHE in disordered semiconductor devices (Kato et al., 2004a) are obtained but for perfectly clean sample, such as: the out-of-plane $\langle S_{\mathbf{m}}^z \rangle$ component of the spin accumulation develops two peaks of opposite signs at the lateral edges of the 2DEG; upon reversing the bias voltage, the edge peaks flip their sign; around the left-lead-2DEG interface $\langle S_{\mathbf{m}}^z \rangle$ is suppressed since unpolarized electrons are injected at this contact. By attaching two additional transverse leads at the lateral edges in Fig. 9(b), we show how spin- \uparrow and spin- \downarrow densities will flow through those leads in opposite directions to generate spin-Hall current, thereby providing an all-electrical semiconductor-based spin injector using ballistic nanostructures with intrinsic SO couplings. No discussion of controversial spin currents within the sample is necessary to reach this conclusion. Note that simple picture of opposite spin densities flowing in opposite directions in Fig. 9(b) is obtained in samples smaller than L_{SO} , while in larger samples these patterns are more complicated (Nikolić et al., 2006) due to multiple spin precession within the sample before spin has a chance to exit through the leads.

The spatial profile of local spin currents corresponding to Fig. 9(b) is shown in Fig. 9(c),(d) where we separate the integration in Eq. (73b) for S_z bond spin current into two parts $\langle \hat{J}_{\mathbf{m}\mathbf{m}'}^{S_z} \rangle = \langle \hat{J}_{\mathbf{m}\mathbf{m}'}^{S_z(\text{eq})} \rangle + \langle \hat{J}_{\mathbf{m}\mathbf{m}'}^{S_z(\text{neq})} \rangle$:

$$\begin{aligned} \langle \hat{J}_{\mathbf{m}\mathbf{m}'}^{S_z} \rangle &= \frac{t_{\text{O}}}{2} \int_{E_b}^{E_F - eV/2} \frac{dE}{2\pi} \text{Tr}_{\text{S}} [\hat{\sigma}_z (\mathbf{G}_{\mathbf{m}'\mathbf{m}}^{\leftarrow}(E) - \mathbf{G}_{\mathbf{m}\mathbf{m}'}^{\leftarrow}(E))] \\ &+ \frac{t_{\text{O}}}{2} \int_{E_F - eV/2}^{E_F + eV/2} \frac{dE}{2\pi} \text{Tr}_{\text{S}} [\hat{\sigma}_z (\mathbf{G}_{\mathbf{m}'\mathbf{m}}^{\leftarrow}(E) - \mathbf{G}_{\mathbf{m}\mathbf{m}'}^{\leftarrow}(E))], \end{aligned} \quad (87)$$

plotted as panels (c) and (d), respectively. The states from the band bottom E_b to $E_F - eV/2$ are fully occupied, while states in the energy interval from the electrochemical potential $E_F - eV/2$ ($eV > 0$) of the right reservoir to the electrochemical potential $E_F + eV/2$ of the left reservoir are partially occupied because of the competition between the left reservoir which tries to fill them and the right reservoir which tries to deplete them. The spatial distribution of the microscopic spin currents in Fig. 9(c) is akin to the vortex-like pattern of bond spin currents within the device that would exist in equilibrium $eV_p = \text{const.}$ (Nikolić et al., 2006). These do not transport any spin between two points in real space since their sum over any cross section is zero. Thus, Fig. 9(d) demonstrates that non-zero spin-Hall flux through the transverse cross sections is due to only the wave functions (or Green functions) around the Fermi energy. The same sum of $\langle \hat{J}_{\mathbf{m}\mathbf{m}'}^{S_z(\text{neq})} \rangle$ in (d) over arbitrary transverse cross section (orthogonal to the y -axis) defines the total spin current which, although not the same on different cross sections within the sample, flows into the leads where it becomes conserved and it is measurable [e.g., via the inverse SHE (Hankiewicz et al., 2004)].

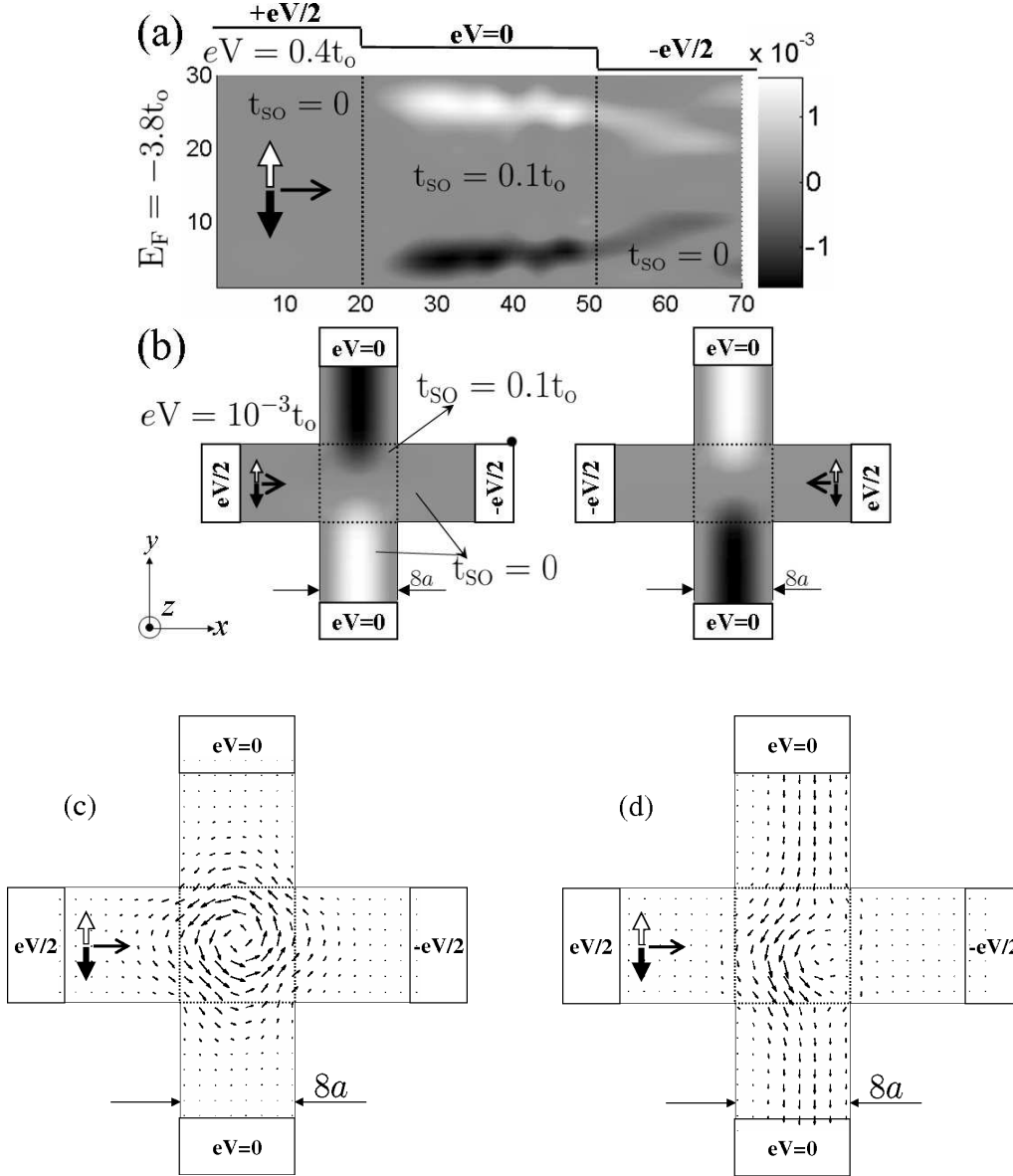


Figure 9: (a) The out-of-plane component $\langle S_m^z \rangle$ of the nonequilibrium spin accumulation induced by nonlinear ($eV = 0.4t_0$) quantum transport of unpolarized charge current injected from the left lead into a two-terminal clean 2DEG nanostructure (of size $L = 30a > L_{SO}$, $a \simeq 3$ nm) with the Rashba SO coupling $t_{SO} = 0.1t_0$ and spin precession length $L_{SO} \approx 15.7a$. (b) Lateral spin- \uparrow and spin- \downarrow densities will propagate in opposite directions through the attached transverse ideal ($t_{SO} = 0$) electrodes to yield a linear response spin-Hall current $I_y^{S_z}$ flowing out of 2DEG ($L = 8a < L_{SO}$), which changes sign upon reversing the bias voltage. (c), (d) The spatial distribution of local spin currents in ballistic four-terminal 2DEG bridges with the Rashba SO coupling $t_{SO} = 0.1t_0$ setting $L_{SO} \approx 15.7a$ and linear response bias voltage $eV = 10^{-3}t_0$. The local spin current is the sum of equilibrium (persistent) spin current in (c), carried by the fully occupied states from $-4t_0$ to $E_F - eV/2$, and the nonequilibrium (transport) spin current in (d) carried by the partially occupied states around the Fermi energy from $\mu_R = E_F - eV/2$ (electrochemical potential of the right reservoir) to $\mu_L = E_F + eV/2$ (electrochemical potential of the left reservoir).

9 COMPUTATIONAL ALGORITHMS FOR REAL \otimes SPIN SPACE NEGFs IN MULTITERMINAL DEVICES

While all formulas in Sec. 8.4 for the core NEGF quantities, $\mathbf{G}(E)$ and $\mathbf{G}^<(E)$, can be implemented by brute force operations on full matrices, this is typically restricted to small lattices of few thousands sites due to computational complexity of matrix operations. For example, for a system of size L in d dimensions, the computing time scales as L^{3d} while the memory needed scales as L^{2d} . By separating system into slices described by much smaller Hamiltonian matrices, and by using the recursive Green function algorithm in serial or parallel implementation (Drouvelis et. al., 2006), the complexity can be reduced drastically to L^{3d-2} scaling of the required computing time.

It is often considered (Kazymyrenko and Waintal, 2008) that the recursive algorithm can be applied only to two-terminal devices and for the computation of total transport quantities in the leads. Some alternative algorithms with reduced computational complexity tailored for multiterminal structures have been proposed recently (Kazymyrenko and Waintal, 2008), and the recursive algorithm has also been extended to get local charge quantities within the sample (Cresti et al., 2003; Metalidis and Bruno, 2005; Lassl et al., 2007). We discuss in Sec. 9.2 how to extend the recursive scheme to four-terminal mesoscopic spin-Hall bridges in Fig. 7 that makes possible computation of the spin-Hall conductance on large lattice sizes shown in Fig. 8(a). In addition, Sec. 9.3 shows how to obtain local spin densities within large two-terminal structures (Nikolić et al., 2005c) using the recursive-type approach. Since the starting point of any algorithm to obtain $\mathbf{G}(E)$ and $\mathbf{G}^<(E)$ for open finite-size system is computation of self-energies for the infinite part (ensuring continuous spectrum and dissipation) of the system in the form of semi-infinite electrodes attached to the finite-size sample, we briefly review recent developments in numerical techniques used to compute the surface Green function of semi-infinite leads that generates matrices for $\Sigma(E)$ and $\Sigma^<(E)$.

9.1 Numerical algorithms for computing self-energy matrices

Several different numerical techniques are available to evaluate single-particle Green function of a semi-infinite electrode using a localized basis (Velev and Butler, 2004). For example, the so-called Ando method (Ando, 1991) computes the surface Green function of a homogeneous lead, consisting of repeating supercell described by the Hamiltonian $\mathbf{H}_{i,i}$ where supercells are coupled by the Hamiltonian $\mathbf{H}_{i,i-1}$, from its exact Bloch propagating modes at energy E . This method offers high precision numerical evaluation of the self-energy and can be generalized (Khomyakov et al., 2005; Rocha et al., 2006) or accelerated (Sørensen et al., 2008) to complicated homogeneous periodic systems where $\mathbf{H}_{i,i-1}$ is not invertible (required in the original Ando algorithm) due to atomistic structure of the leads or more complicated than square tight-binding lattice [such as the honeycomb one (Chen et al., 2007; Zârbo and Nikolić, 2007)].

An alternative and approximate method, applicable also to inhomogeneous systems (when the lead does not consist of repeating supercells with identical $\mathbf{H}_{i,i}$), is the recursive (or continued fraction) algorithm for the surface Green function (Velev and Butler, 2004). It connects Green function of a given layer to Green functions of neighboring layers, so that

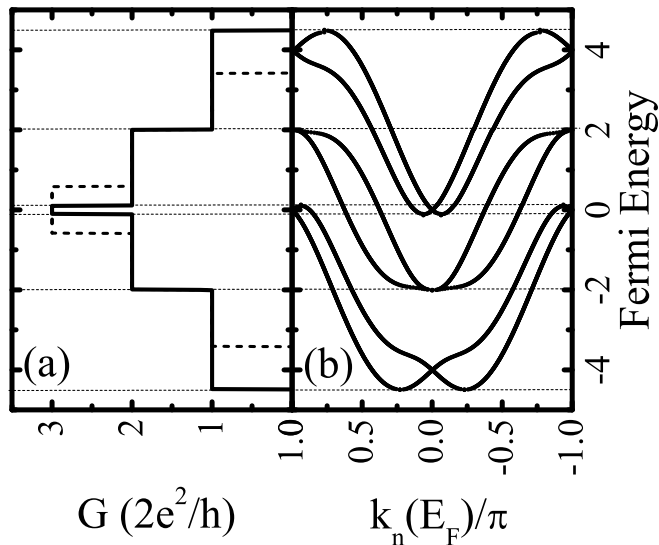


Figure 10: The conductance quantization (a) in the Rashba spin-split infinite clean quantum wire modeled on the lattice with three sites per cross section. The wire is decomposed into the finite-size central sample attached to two semi-infinite leads where the Rashba hopping $t_{SO} = t_O$ exists in all three segments. The dashed line in (a) corresponds to quantized conductance of the same wire in the absence of the SO coupling $t_{SO} = 0$. Panel (b) plots the Rashba-split subband dispersion responsible for this unusual conductance quantization.

starting from the surface layer and repeating this process until the effect of all other layers on the surface layer is taken account yields the surface Green function (in practice, the recursive method is executed to finite depth into the lead where the number of considered neighboring layers affecting the surface layer is set by the convergence criterion).

The Ando method can be executed analytically for simple square lattice lead with no SO coupling (Datta, 1995). For comparing mesoscopic SHE calculations to the bulk SHE description, it is also useful to have a system where SO-coupled leads are attached to identical SO-coupled sample to form an infinite spin-split wire, while two additional ideal (with no spin interactions) leads are attached in the transverse direction (Sheng and Ting, 2006). The self-energies for semi-infinite electrodes with the Rashba SO coupling can be obtained via the Ando method, with doubled size matrices $\mathbf{H}_{i,i}$ and $\mathbf{H}_{i,i-1}$ to include spin. We employ this method in Fig. 10 to provide a simple example of the conductance quantization through three-channel infinite spin-split quantum wire that can be used as a building block of the four-terminal calculations. The Rashba-split subbands define new conducting channels whose spin polarization properties can be highly nontrivial for strong SO coupling (Governale and Zülicke, 2004), as discussed in Sec. 6.2.1. This is in contrast to standard wires where conducting channels are always separable states $|n\rangle \otimes |\sigma\rangle$, which simplifies the analysis of spin injection (Nikolić and Souma, 2005a) while also introducing the scattering at the lead-sample interface which can reduce the spin-Hall conductance (Nikolić et al., 2005b; Sheng and Ting, 2006).

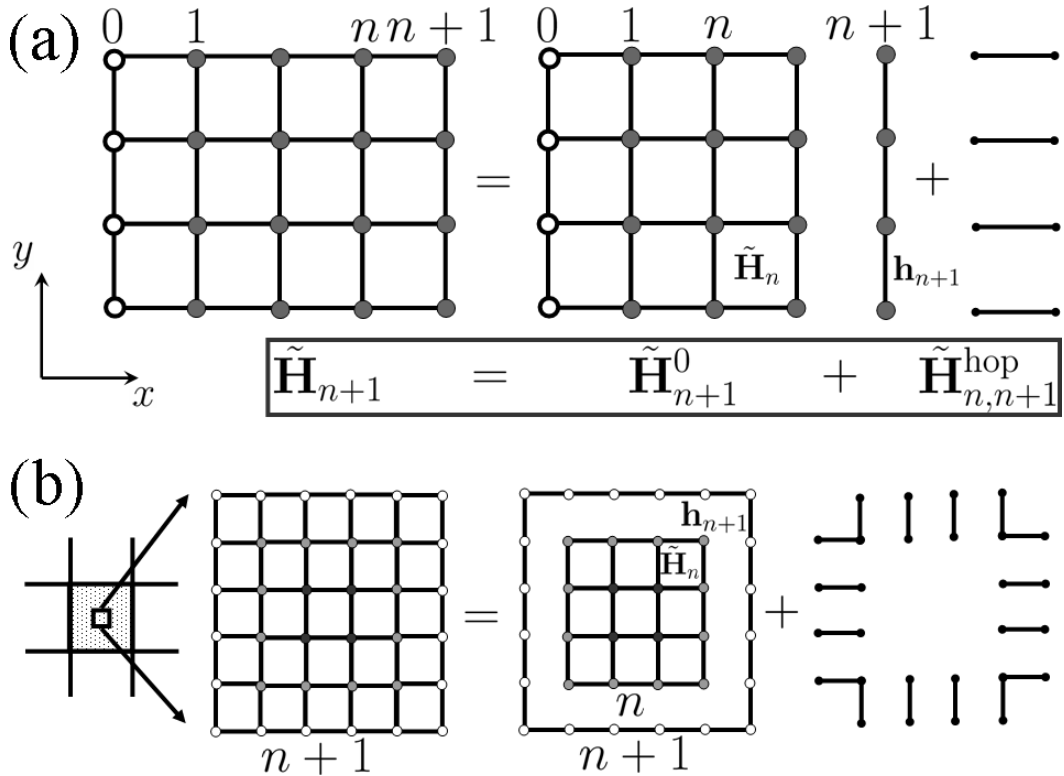


Figure 11: Illustration of the recursive Green function computational algorithm for: a) two-terminal setup; and b) four-terminal setup defined on the square tight-binding lattice.

9.2 Recursive Green function algorithm for total spin and charge currents in multiterminal nanostructures

For many transport calculations the full retarded Green function Eq. (82) is not required. For instance, to compute the transmission matrix (49) from lead q to lead p , one only needs the Green function matrix elements $(\mathbf{G})_{\mathbf{m}\mathbf{m}',\sigma\sigma'}$ where the sites \mathbf{m} belong to the lead p edge supercell and the sites \mathbf{m}' belong to the first supercell of the lead q . We first discuss the recursive algorithm (Drouvelis et. al., 2006) that evaluates only this portion $\mathbf{G}_{N+1,0}$ of the full retarded Green function matrix for the two-probe setup in Fig. 11(a). The sample is divided into N layers, and to account for the effect of the leads, their self-energies are added onto the layers 0 and $N + 1$. These two layers are the first principal layers of the two leads. It is important to emphasize that adding the self-energies directly onto the sample in more complicated cases than simple square lattice can lead to incorrect result for the transmission eigenvalues.

The recursive scheme starts by adding the self-energy of the left lead Σ_L onto its principal layer directly connected to the sample. The Hamiltonian of any of the $N + 2$ blocks is labeled by \mathbf{h}_n . The retarded Green function matrix of the n -th isolated block is $\mathbf{g}_n = (E - \mathbf{h}_n - i\eta)^{-1}$. The hopping matrix connecting blocks n and $n + 1$ is

$$\mathbf{H}_{n,n+1}^{\text{hop}} = \begin{pmatrix} 0 & \mathbf{H}_{n,n+1} \\ \mathbf{H}_{n+1,n} & 0 \end{pmatrix}. \quad (88)$$

We also introduce $\tilde{\mathbf{H}}_n$ as the matrix which is the sum of the Hamiltonian of $n + 1$ blocks and the lead self-energy added to the 0-th block. The corresponding retarded Green function matrix is $\mathbf{G}_n = (E - \tilde{\mathbf{H}}_n + i\eta)^{-1}$. One can add the next isolated block \mathbf{h}_{n+1} to $\tilde{\mathbf{H}}_n$ and obtain $\tilde{\mathbf{H}}_{n+1}^{(0)} = \tilde{\mathbf{H}}_n \oplus \mathbf{h}_{n+1}$.

Assuming that the Green function of n blocks is known, we add the $n + 1$ -th block to $\tilde{\mathbf{H}}_n$ without turning on the coupling $\mathbf{H}_{n,n+1}^{\text{hop}}$ between them. The new Hamiltonian, is block diagonal

$$\tilde{\mathbf{H}}_{n+1}^{(0)} = \begin{pmatrix} \tilde{\mathbf{H}}_n & 0 \\ 0 & \mathbf{h}_{n+1} \end{pmatrix}, \quad (89)$$

whose inversion leads to

$$\mathbf{G}_{n+1}^{(0)} = \begin{pmatrix} \mathbf{G}_n & 0 \\ 0 & \mathbf{g}_{n+1} \end{pmatrix}. \quad (90)$$

To find the Green function \mathbf{G}_{n+1} it is necessary to add the matrix elements connecting the $n + 1$ -th block to $\tilde{\mathbf{H}}_n$

$$\tilde{\mathbf{H}}_{n+1} = \begin{pmatrix} \tilde{\mathbf{H}}_n & \mathbf{H}_{n,n+1} \\ \mathbf{H}_{n+1,n} & \mathbf{h}_{n+1} \end{pmatrix}. \quad (91)$$

The Green function of $n + 2$ blocks can be found by using the Dyson equation

$$\mathbf{G}_{n+1} = \mathbf{G}_{n+1}^{(0)} + \mathbf{G}_{n+1}^{(0)} \mathbf{H}_{n,n+1}^{\text{hop}} \mathbf{G}_{n+1}. \quad (92)$$

All matrices in this equation are of the dimension $n + 2$ in the block coordinate space. Equation (92) can be used to obtain the recurrence relationships for the Green function blocks we are interested in. To get the conductance of the two-terminal device we need to compute $\langle N + 1 | \mathbf{G}_{N+1} | 0 \rangle \equiv \mathbf{G}_{N+1}(N + 1, 0)$ which connects the right and the left lead.

In the multiterminal case, we choose to start from the Hamiltonian of the block of sites in the center of the sample and then add one-by-one additional blocks of the same shape until we reaches the attached electrodes, as sketched in Fig. 11(b). Therefore, in this case we need the Green function elements $\mathbf{G}_{N+1}(N + 1, N + 1)$. From Eq. (92) we find

$$\mathbf{G}_{n+1}(n + 1, n + 1) = \mathbf{G}_{n+1}^{(0)}(n + 1, n + 1) + \left\langle n + 1 \left| \mathbf{G}_{n+1}^{(0)} \mathbf{H}_{n,n+1}^{\text{hop}} \mathbf{G}_{n+1} \right| n + 1 \right\rangle. \quad (93)$$

By inserting the identity matrix in the subspace of block coordinates into Eq. (93)

$$\mathbf{I} = \sum_m |m\rangle \langle m|, \quad (94)$$

the second term in Eq. (93) becomes

$$\left\langle n + 1 \left| \mathbf{G}_{n+1}^{(0)} \sum_m |m\rangle \langle m| \mathbf{H}_{n,n+1}^{\text{hop}} \sum_m |l\rangle \langle l| \mathbf{G}_{n+1} \right| n + 1 \right\rangle. \quad (95)$$

It is easy to see from Eqs. (88), (90), and (91) that

$$\langle n + 1 | \mathbf{G}_{n+1}^{(0)} | m \rangle = \delta_{n+1,m} \mathbf{g}_{n+1}, \quad (96a)$$

$$\langle m | \mathbf{H}_{n,n+1}^{\text{hop}} | l \rangle = \delta_{m,n} \delta_{l,n+1} \mathbf{H}_{n,n+1} + \delta_{m,n+1} \delta_{l,n} \mathbf{H}_{n+1,n}. \quad (96b)$$

Equation (96) can be substituted into Eq. (95) to yield the Dyson Eq. (92) for $\mathbf{G}_{n+1}(n+1, n+1)$

$$\mathbf{G}_{n+1}(n+1, n+1) = \mathbf{g}_{n+1} + \mathbf{g}_{n+1} \mathbf{H}_{n+1, n} \mathbf{G}_{n+1}(n, n+1), \quad (97)$$

in which $\mathbf{G}_{n+1}(n, n+1)$ is an unknown quantity. By computing the matrix elements of the terms in the Dyson Eq. (92) between $|n\rangle$ and $|n+1\rangle$ we find that

$$\mathbf{G}_{n+1}(n, n+1) = \mathbf{G}_n(n, n) \mathbf{H}_{n, n+1} \mathbf{G}_{n+1}(n+1, n+1). \quad (98)$$

Finally, combining Eqs. (97) and (98) leads the following recurrence relationship

$$\mathbf{G}_{n+1}(n+1, n+1) = \frac{\mathbf{I}_{n+1}}{\mathbf{g}_{n+1}^{-1} - \mathbf{H}_{n+1, n} \mathbf{G}_n(n, n) \mathbf{H}_{n, n+1}}. \quad (99)$$

Here the matrix \mathbf{I}_{n+1} is the identity matrix in the subspace of the $n+1$ -th block and the denominator is the matrix to be inverted.

If the recursive scheme in Fig. 11(b) is used, we need to obtain $\mathbf{G}_{N+1}(N+1, N+1)$ from which the transmission matrix can be computed. For the two-terminal case, the recursive scheme sketched in Fig. 11(a) is more efficient computationally. Computing the matrix elements of the Dyson Eq. (92) between the states $|n+1\rangle$ and $|m\rangle$ gives

$$\mathbf{G}_{n+1}(n+1, m) = \mathbf{G}_{n+1}(n+1, n+1) \mathbf{H}_{n+1, n} \mathbf{G}_n(n, m) \quad (100)$$

where $m < n+1$.

We summarize the general recursive Green function algorithm for the computation of (spin-resolved) transmissions, and therefore spin or charge conductances, in the form of the following steps:

1. Calculate the self-energies for the leads, as described in Section 9.1.
2. Identify the $N+2$ blocks for the recursive method as shown in Fig. 11 (the number of sites of each block might be different).
3. Initialize the recurrence by computing $\mathbf{G}_0(0, 0) \equiv \mathbf{g}_0$, where $\mathbf{g}_0 = (E - \tilde{\mathbf{H}}_0 - i\eta)^{-1}$ is the Green function of the first block. This block has the self-energy added to it in the two-terminal case. In the multiterminal case, the first block can be chosen to be a rectangle of the size $N_x^{(0)} \times N_y^{(0)}$ sites, as illustrated in Fig. 11(b). A difficulty may arise in the multiterminal cases where the matrix $E - \mathbf{h}_0$ can turn to be singular for certain choices of the shape of the sample or its parameters.
4. Using the formulas (99) and (100) compute the Green functions $\mathbf{G}_{N+1}(N+1, N+1)$ and $\mathbf{G}_{N+1}(N+1, 0)$.
5. Obtain the retarded Green function matrix elements \mathbf{G}_{pq} connecting each pair of leads p and q , either from $\mathbf{G}_{N+1}(N+1, 0)$ in the two-terminal case, or $\mathbf{G}_{N+1}(N+1, N+1)$ in the multiterminal case.
6. Compute the transmission matrix using Eq. (49).

9.3 Recursive Green function algorithm for local spin and charge densities

The computation of nonequilibrium spin and charge densities using Eq. (80) and (70), respectively, requires to obtain $\mathbf{G}^<$. This has the highest computational complexity since one has to perform the matrix multiplication in Eq. (81). Moreover, this matrix multiplication has to be done for all the energy points in Eq. (80). Here we introduce a method for recursive calculation of the spin and charge nonequilibrium densities within the NEGF formalism which makes it possible to greatly reduce this computational complexity and, thereby, analyze spin densities in sizable samples (Nikolić et al., 2005c).

In order to illustrate the essential steps of this method, it is enough to consider a simple two-probe setup in Fig. 11(a). The two-probe system considered here is made of $N + 2$ blocks, where the 0-th block is the first left lead supercell onto which the left lead self-energy is added, and $N + 1$ -th block is the first right lead supercell onto which the right lead self-energy is added. The voltage applied onto the left and right lead is V_L and V_R , respectively. The lesser self-energy matrix in Eq. (81) can be rewritten as

$$\begin{aligned} \Sigma^<(E) &= i\mathbf{\Gamma}_L(E - eV_L)f(E - eV_L) + i\mathbf{\Gamma}_R(E - eV_R)f(E - eV_R) \\ &= \begin{pmatrix} i\mathbf{\Gamma}_L(E - eV_L)f(E - eV_L) & \dots & 0 \\ \dots & \dots & \dots \\ 0 & \dots & i\mathbf{\Gamma}_R(E - eV_R)f(E - eV_R) \end{pmatrix}. \end{aligned} \quad (101)$$

where the only non-zero elements are the first and the last on the diagonal. This simplifies greatly the matrix multiplication in Eq. (81), since only multiplication by the non-zero matrix elements of $\Sigma^<$ is required

$$\Sigma^<(0, 0) = i\mathbf{\Gamma}_L(E - eV_L)f(E - eV_L), \quad (102a)$$

$$\Sigma^<(N + 1, N + 1) = i\mathbf{\Gamma}_R(E - eV_R)f(E - eV_R). \quad (102b)$$

In order to calculate the nonequilibrium spin density Eq. (80) or charge density Eq. (70), only the diagonal elements of $\mathbf{G}^<(E)$ are required. Using Eqs. (101) and (102) in Eq. (81), leads to

$$\begin{aligned} \mathbf{G}^<(m, m) &= \mathbf{G}(m, N + 1)\Sigma^<(N + 1, N + 1)\mathbf{G}^\dagger(N + 1, m) \\ &+ \mathbf{G}(m, 0)\Sigma^<(0, 0)\mathbf{G}^\dagger(0, m), \end{aligned} \quad (103)$$

where m labels the coordinates of the m -th block.

The retarded Green function matrices $\mathbf{G}(m, N + 1)$ and $\mathbf{G}(m, 0)$ can be found using the Dyson Eq. (92) introduced in Sec. 9.2. To find $\mathbf{G}(m, N + 1)$, one starts the recurrence from the left lead and finds

$$\mathbf{G}_{n+1}(m, n + 1) = \mathbf{G}_n(m, n)\mathbf{H}_{n,n+1}\mathbf{G}_{n+1}(n + 1, n + 1), \quad (104)$$

where $m \leq n$. The Green function block $\mathbf{G}_{n+1}(n + 1, n + 1)$ can be obtained from Eq. (99). To find $\mathbf{G}(m, 0)$, the recurrence has to start from the right lead and we get

$$\mathbf{G}_{n-1}(m, n - 1) = \mathbf{G}_n(m, n)\mathbf{H}_{n,n-1}\mathbf{G}_{n-1}(n - 1, n - 1), \quad (105)$$

where $m \geq n$. The system of equations is finally closed by using

$$\mathbf{G}_{n-1}(n-1, n-1) = \frac{\mathbf{I}_{n-1}}{\mathbf{g}_{n-1}^{-1} - \mathbf{H}_{n-1,n} \mathbf{G}_n(n, n) \mathbf{H}_{n,n-1}}. \quad (106)$$

In this method, one has to compute recursively the retarded Green functions $\mathbf{G}(m, N+1)$ and $\mathbf{G}(m, 0)$ for all $m = \overline{0, N+1}$. It is not as computationally costly as the full Green function matrix inversion, and it can be extended to compute bond spin and charge currents. In that case, we also have to find $\mathbf{G}(m \pm 1, N+1)$ and $\mathbf{G}(m \pm 1, 0)$.

10 CONCLUDING REMARKS

The pure spin currents, which arise when equal number of spin- \uparrow and spin- \downarrow electrons propagate in opposite directions so that net charge current carried by them is zero, have recently emerged as one of the major topics of both metal and semiconductor-based spintronics. This is due to the fact that they offer new realm to explore fundamental spin transport phenomena in solids, as well as to construct new generation of spintronic devices with greatly reduced power dissipation and new functionality in transporting either classical or quantum (such as flying spin qubits) information. Their generation (which is currently experimentally achieved mostly through spin pumping, non-local spin injection using lateral spin valves, and SHE), control, and demanding detection typically involves quantum-coherent spin dynamics. In particular, the recently discovered SHE and the inverse SHE have offered some of the most efficient scheme to generate and detect pure spin currents, respectively. However, they have also posed numerous challenges for their theoretical description and device modeling since conventionally defined spin current operator does not satisfy standard continuity equation for spin when intrinsic SO couplings (which act as homogeneous internal momentum-dependent magnetic fields affecting the band structure and causing spin precession) are present. Even with modified spin current definitions, this fundamental problem makes difficult easy connection between theoretically computed spin conductivities of infinite homogeneous systems and usually experimentally measured spin densities for devices with arbitrary boundaries and attached external electrodes. An attempt to give up on the theoretical description of spin flow through spin current altogether, by using spin density within the diffusion equation formalism (which is expected to provide a complete and physically meaningful description of spin and charge diffusive transport in terms of position and time dependent spin and charge densities), leads to another set of obstacles. That is, the explicit solution of the diffusion equation strongly depends on the boundary conditions (extracted for charge diffusion from conservation laws) where spin non-conservation, manifested as ballistic spin precession at the edges, cannot be unambiguously matched with the diffusive dynamics in the bulk captured by the diffusion equation for length scales much longer than the mean free path.

This chapter of the Handbook provides a summary of such fundamental problems in spin transport through SO-coupled semiconductors and possible resolution through spin-dependent NEGF formalism that can handle *both* ballistic and diffusive regimes, as well as phase-coherent and dephasing effects, in realistic multiterminal nanostructures operating at different mobilities and temperatures. The central quantities of this approach—total spin currents flowing out of the device through ideal (interaction free) electrodes, local spin densities within the

sample and along the edges, and local spin currents (whose sums within the leads gives total spin currents)—can be used to understand experiments or model novel spintronics devices. For example, NEGF approach is indispensable (Hankiewicz et al., 2004) for computational modeling of generator-detector experimental setups (Brüne et al., 2008; Roth et al., 2009) where direct and inverse SHE multiterminal bridges are joined into a single circuit to sense the pure spin-Hall current through voltages induced by its flow through regions with SO interactions. The chapter also provides extensive coverage of relevant technical and computational details, such as: the construction of retarded and lesser nonequilibrium Green functions for SO-coupled nanostructures attached to many electrodes; computation of relevant self-energies introduced by the lead-sample interaction; and accelerated algorithms which make possible spin transport modeling in device whose size is comparable to the spin precession length of few hundreds of nm where SHE response to injected unpolarized charge current is expected to be optimal (Nikolić et al., 2005*b*; Moca and Marinescu, 2007).

Acknowledgments

We acknowledge numerous insightful discussions with Í. Adagideli, S. Datta, J. Fabian, J. Inoue, S. Murakami, N. Nagaosa, J. Nitta, K. Nomura, M. Onoda, E. I. Rashba, and J. Sinova. This work was supported by NSF Grant No. ECCS 0725566, DOE Grant No. DE-FG02-07ER46374, and the Center for Spintronics and Biodetection at the University of Delaware.

References

- Adagideli, Í., and Bauer, G. E. W. (2005) *Phys. Rev. Lett.* **95** 256602.
- Adagideli, Í., Bauer, G. E. W. and Halperin, B. I. (2006) *Phys. Rev. Lett.* **97** 256601.
- Aleiner, I. L., and Fal’ko, V. I. (2001) *Phys. Rev. Lett.* **87** 256801.
- Ando, T. (1991) *Phys. Rev. B* **44** 8017.
- Ando, T. (2003) *Physica E* **20** 24.
- Awschalom, D. D. and Flatté, M. E. (2007) *Nature Phys.* **3** 153.
- Ballentine, L. E. (1998) *Quantum Mechanics: A Modern Development*, World Scientific, Singapore.
- Baranger, H. U. and Stone, A. D. (1989) *Phys. Rev. B* **40** 8169.
- Bardarson, J. H., Adagideli, Í and Jacquod, P. (2007) *Phys. Rev. Lett.* **98** 196601.
- Bleibaum, O. (2006) *Phys. Rev. B* **74** 113309.
- Brüne, C., Roth, A., Novik, E. G., König, M., Buhmann, H., Hankiewicz, E. M., Hanke, W., Sinova, J. and Molenkamp, L. W. (2008) preprint [arXiv:0812.3768](https://arxiv.org/abs/0812.3768).

- Bulgakov, E. N., Pichugin, K. N., Sadreev, A. F., Středa, P. and Šeba, P. (1999) Phys. Rev. Lett. **83** 376.
- Burkov, A. A., Núñez, A. S. and MacDonald, A. H. (2004) Phys. Rev. B **70** 155308.
- Büttiker, M. (1986) Phys. Rev. Lett. **57** 1761.
- Caroli, C., Combescot, R., Nozieres, P. and Saint-James, D. (1971) J. Phys. C: Solid State Phys. **4** 916.
- Chang, C. H., Mal'shukov, A. G. and Chao, K. A. (2004) Phys. Rev. B **70** 245309.
- Chen, S.-H., Liu M.-H. and Chang, C.-R. (2007) Phys. Rev. B **76** 075322.
- Chen, S.-H., Chang, C.-R., Xiao, J. Q. and Nikolić, B. K. (2009) Phys. Rev. B **79** 054424.
- Costache, M. V., Sladkov, M., Watts, S. M., van der Wal, C. H. and van Wees, B. J. (2006) Phys. Rev. Lett. **97** 216603.
- Christen, T. and Büttiker, M. (1996) Europhys. Lett. **35** 523.
- Cresti, A., Farchioni, R., Grosso, G. and Parravicini, G. P. (2003) Phys. Rev. B **68** 075306.
- Crooker, S. A. and Smith, D. L. (2005) Phys. Rev. Lett. **94** 236601.
- Datta, S. and Das, B. (1990) Appl. Phys. Lett. **56** 665.
- Datta, S. (1995) *Electronic Transport in Mesoscopic Systems*, Cambridge University Press, Cambridge.
- Datta, S. (2005) *Quantum Transport: Atom to Transistor*, Cambridge University Press, Cambridge.
- Dragomirova, R. L. and Nikolić, B. K. (2007) Phys. Rev. B **75** 085328.
- Dragomirova, R. L., Zârbo, L. P. and Nikolić, B. K. (2008) EPL (Europhys. Lett.) **84** 37004.
- Drouvelis, P.S., Schmelcher, P. and Bastian, P. (2006) J. Comp. Phys. **215** 741.
- D'yakonov, M. I. and Perel', V. I. (1971) Sov. Phys. JETP **13** 467.
- Engel, H. A., Rashba, E. I. and Halperin, B. I. (2007) *Handbook of Magnetism and Advanced Magnetic Materials*, (Ed. H. Kronmüller and S. Parkin) Wiley, Hoboken NJ.
- Fabian, J., Matos-Abiaguea, A., Ertlera, C., Stano, P. and Žutić, I. (2007) Acta Physica Slovaca **57** 565.
- Finkler, I. G., Engel, H. A., Rashba, E. I. and Halperin, B. I. (2007) Phys. Rev. B **75** 241202.
- Fisher, G. P. (1971) Am. J. Phys. **39** 1528.
- Galitski, V. M., Burkov, A. A. and Das Sarma, S. (2006) Phys. Rev. B **74** 115331.

- Ganichev, S. D. and Prettl, W. (2003) *J. Phys.: Condens. Matter* **15** R935.
- Ganichev, S. D., Danilov, S. N., Schneider, P., Bel'kov, V. V., Golub, L. E., Wegscheider, W., Weiss, D. and Prettl, W. (2006) *J. Magn. Magn. Mater.* **300** 127.
- Golizadeh-Mojarad, R. and Datta, S. (2007*a*) *Phys. Rev. B* **75** 081301.
- Golizadeh-Mojarad, R. and Datta, S. (2007*b*) preprint [arXiv:cond-mat/0703280](https://arxiv.org/abs/cond-mat/0703280).
- Governale, M. and Zülicke, U. (2004) *Solid State Comm.* **153** 581.
- Grundler, D. (2000) *Phys. Rev. Lett.* **84** 6074.
- Guo, G. Y., Murakami, S., Chen, T. W. and Nagaosa, N. (2008) *Phys. Rev. Lett.* **100** 096401.
- Hankiewicz, E. M., Molenkamp, L. W., Jungwirth, T. and Sinova, J. (2004) *Phys. Rev. B* **70** 241301.
- Hankiewicz, E. M., Li, J., Jungwirth, T., Niu, Q., Shen, S. and Sinova, J. (2005) *Phys. Rev. B* **72** 155305.
- Hankiewicz, E. M. and Vignale, G. (2008) *Phys. Rev. Lett.* **100** 026602.
- Hanson, R., Kouwenhoven, L. P., Petta, J. R., Tarucha, S. and Vandersypen, L. M. K. (2007) *Rev. Mod. Phys.* **79** 1217.
- Haug, H. and Jauho, A. P. (2007) *Quantum Kinetics in Transport and Optics of Semiconductors* (2nd Ed.), Springer, Berlin.
- Hirsch, J. E. (1999) *Phys. Rev. Lett.* **83** 1834.
- Holleitner, A. W., Sih, V., Myers, R. C., Gossard, A. C. and Awschalom, D. D. (2006) *Phys. Rev. Lett.* **97** 036805.
- Huang, B., Monsma, D. J. and Appelbaum, I. (2007) *Phys. Rev. Lett.* **99** 177209.
- Inoue, J., Bauer, G. E. W. and Molenkamp, L. W. (2004) *Phys. Rev. B* **70** 041303.
- Jackson, J. D. (1998) *Classical Electrodynamics* (3rd Ed.), Wiley, Hoboken NJ.
- Jung, S. and Lee, H. (2005) *Phys. Rev. B* **71** 125341.
- Jungwirth, T., Sinova, J., Mašek J., Kučera, J. and MacDonald, A. H. (2006) *Rev. Mod. Phys.* **78** 809.
- Kato, Y. K., Myers, R. C., Gossard, A. C. and Awschalom, D. D. (2004*a*) *Science* **306** 1910.
- Kato, Y., Myers, R. C., Gossard, A. C. and Awschalom, D. D. (2004*b*) *Nature* **427** 50.
- Kato, Y. K., Myers, R. C., Gossard, A. C. and Awschalom, D. D. (2005) *Appl. Phys. Lett.* **87** 022503.

- Kazymyrenko, K. and Waintal, X. (2008) Phys. Rev. B **77** 115119.
- Keldysh, L. (1965) Sov. Phys. JETP **20** 1018.
- Keyes, R. W. (2005) Rep. Prog. Phys. **68** 2701.
- Khomyakov, P. A., Brocks, G., Karpan, V., Zwierzycki, M. and Kelly, P. J. (2005) Phys. Rev. B **72** 035450.
- Kimura, T., Otani, Y., Sato, T., Takahashi, S. and Maekawa, S., (2007) Phys. Rev. Lett. **98** 156601.
- Kiselev, A. A. and Kim, K. W. (2005) Phys. Rev. B **71** 153315.
- Koentopp, M., Chang, C., Burke, K. and Car, R. (2008) J. Phys.: Condens. Matter **20** 083203.
- König, M., Buhmann, H., Molenkamp, L. W., Hughes, T., Liu, C. X., Qi, X. L. and Zhang, S. C. (2008) J. Phys. Soc. Jpn. **77** 031007.
- Lassl, A., Schlagheck, P. and Richter, K. (2007) Phys. Rev. B **75** 045346.
- van Leeuwen, R., Dahlen, N. E., Stefanucci, G., Almladh, C.-O. and von Barth U. (2006) *Lecture Notes in Physics 706* 33, Springer, Berlin.
- Li, J., Dai, X., Shen, S. and Zhang, F. (2006) Appl. Phys. Lett. **88** 162105.
- Liu, M.-H., G. Bihlmayer, Blögel, S. and Chang, C.-R. (2007) Phys. Rev. B **76** 121301(R).
- Maekawa, S. and Shinjo, T. Eds. (2002) *Spin Dependent Transport in Magnetic Nanostructures*, Taylor and Francis, London.
- Mal'shukov, A. G., Tang, C. S., Chu, C. S. and Chao, K. A. (2005) Phys. Rev. Lett. **95** 107203.
- Meier, F. and Loss, D. (2003) Phys. Rev. Lett. **90** 167204.
- Metalidis, G. and Bruno, P. (2005) Phys. Rev. B **72** 235304.
- Mishchenko, E. G., Shytov, A. V. and Halperin, B. I. (2004) Phys. Rev. Lett. **93** 226602.
- Moca, C. P. and Marinescu, D. C. (2007) Phys. Rev. B **75** 035325.
- Moriyama, T., Cao, R., Fan, X., Xuan, G., Nikolić, B. K., Tserkovnyak, Y., Kolodzey, J. and Xiao, J. Q. (2008) Phys. Rev. Lett. **100** 067602.
- Murakami, S., Nagaosa, N. and Zhang, S. C. (2003) Science **301** 1348.
- Murakami, S. (2006) *Advances in Solid State Physics 45* 197, Springer, Berlin.
- Nagaosa, N. (2008) J. Phys. Soc. Jpn. **77** 031010.
- Nikolić, B. and Allen, P. B. (1999) Phys. Rev. B **60** 3963.

- Nikolić, B. K. and Souma, S. (2005*a*) Phys. Rev. B **71** 195328.
- Nikolić, B. K., Zârbo, L. P. and Souma, S. (2005*b*) Phys. Rev. B **72** 075361.
- Nikolić, B. K., Souma, S., Zârbo, L. P. and Sinova, J. (2005*c*) Phys. Rev. Lett. **95** 046601.
- Nikolić, B. K., Zârbo, L. P. and Souma, S. (2006) Phys. Rev. B **73** 075303.
- Nikolić, B. K. and Zârbo, L. P. (2007) EPL (Europhys. Lett.) **77** 47004.
- Nikolić, B. K. and Dragomirova, R. L. (2009) Semicond. Sci. Tech. **24** 064006.
- Nitta, J., Akazaki, T., Takayanagi, H. and Enoki, T. (1997) Phys. Rev. Lett. **78** 1335.
- Nomura, K., Wunderlich, J., Sinova, J., Kaestner, B., MacDonald, A. H. and Jungwirth, T. (2005) Phys. Rev. B **72** 245330.
- Nonoyama, S. and Oguri, A. (1998) Phys. Rev. B **57** 8797.
- Okamoto, S. (2007) Phys. Rev. B **76** 035105.
- Onoda, M. and Nagaosa, N. (2005*a*) Phys. Rev. B **72** 081301.
- Onoda, M. and Nagaosa, N. (2005*b*) Phys. Rev. Lett. **95** 106601.
- Pareek, T. P. (2004) Phys. Rev. Lett. **92** 076601.
- Ralph, D. and Stiles, M. (2008) J. Mag. Mag. Mater. **320** 1190.
- Rammer, J. (2007) *Quantum Field Theory of Non-Equilibrium States*, Cambridge University Press, Cambridge.
- Rashba, E. I. (2003) Phys. Rev. B **68** 241315.
- Ren, W., Qiao, Z., Wang, J., Sun, Q. and Guo, H. (2006) Phys. Rev. Lett. **97** 066603.
- Reynoso, A., Usaj, G. and Balseiro, C. A. (2006) Phys. Rev. B **73** 115342.
- Rocha, A. R., García-Suárez, V. M., Bailey, S., Lambert, C., Ferrer, J. and Sanvito, S. (2006) Phys. Rev. B **73** 085414.
- Roth, A., Brüne, C., Buhmann, H., Molenkamp, L. W., Maciejko, J., Qi, X.-L., and Zhang, S.-C. (2009) preprint [arXiv:0905.0365](https://arxiv.org/abs/0905.0365).
- Saitoh, E., Ueda, M., Miyajima, H. and Tataru, G. (2006) Appl. Phys. Lett. **88** 182509.
- Scheid, M., Bercieux, D. and Richter, K. (2007) New J. Phys. **9** 401.
- Schliemann, J. (2006) Int. J. Mod. Phys. B **20** 1015.
- Sharma, P. (2005) Science **307** 531.

- Sheng, L., Sheng, D. N., Ting, C. S. and Haldane, F. D. M. (2005) *Phys. Rev. Lett.* **95** 136602.
- Sheng, L. and Ting, C. S. (2006) *Int. J. Mod. Phys. B* **20** 2339.
- Shi, J., Zhang, P., Xiao, D. and Niu, Q. (2006) *Phys. Rev. Lett.* **96** 076604.
- Sih, V., Myers, R. C., Kato, Y. K., Lau, W. H., Gossard, A. C. and Awschalom, D. D. (2005) *Nature Phys.* **1** 31.
- Sih, V., Lau, W. H., Myers, R. C., Horowitz, V. R., Gossard, A. C. and Awschalom, D. D. (2006) *Phys. Rev. Lett.* **97** 096605.
- Silov, A. Y., Blajnov, P. A., Wolter, J. H., Hey, R., Ploog, K. H. and Averkiev, N. S. (2004) *Appl. Phys. Lett.* **85** 5929.
- Silsbee, R. H. (2004) *J. Phys.: Condens. Matter* **16** 179.
- Silvestrov, P. G., Zyuzin, V. A. and Mishchenko, E. G. (2009) *Phys. Rev. Lett.* **102** 196802.
- Sinitsyn, N. A. (2008) *J. Phys.: Condens. Matter* **20** 023201.
- Sinova, J., Culcer, D., Niu, Q., Sinitsyn, N. A., Jungwirth, T. and MacDonald, A. H. (2004) *Phys. Rev. Lett.* **92** 126603.
- Sinova, J., Murakami, S., Shen, S.-Q. and Choi, M.-S. (2006) *Solid State Comm.* **138** 214.
- Sørensen, H. H. B., Hansen, P. C., Petersen, D. E., Skelboe, S. and Stokbro, K. (2008) *Phys. Rev. B* **77** 155301.
- Souma, S. and Nikolić, B. K. (2004) *Phys. Rev. B* **70** 195346.
- Souma, S. and Nikolić, B. K. (2005) *Phys. Rev. Lett.* **94** 106602.
- Stern, N. P., Ghosh, S., Xiang, G., Zhu, M., Samarth, N. and Awschalom, D. D. (2006) *Phys. Rev. Lett.* **97** 126603.
- Stevens, M. J., Smirl, A. L., Bhat, R. D. R., Najmaie, A., Sipe, J. E. and van Driel, H. M. (2003) *Phys. Rev. Lett.* **90** 136603.
- Sugimoto, N., Onoda, S., Murakami, S. and Nagaosa, N. (2006) *Phys. Rev. B* **73** 113305.
- Tang, C. S. (2006) *Int. J. Mod. Phys. B* **20** 869.
- Thygesen, K. S. and Rubio, A. (2008) *Phys. Rev. B* **77** 115333.
- Todorov, T. N. (2002) *J. Phys.: Condens. Matter* **14** 3049.
- Topinka, M. A., Westervelt, R. M. and Heller, E. J. (2003) *Phys. Today* **56(12)** 47.
- Tserkovnyak, Y., Brataas, A., Bauer, G. E. W. and Halperin, B. I. (2005) *Rev. Mod. Phys.* **77** 1375.

- Tserkovnyak, Y. and Brataas, A. (2007) Phys. Rev. B **76** 155326.
- Valenzuela, S. O. and Tinkham, M. (2006) Nature **442** 176.
- Velev, J. and Butler, W. (2004) J. Phys: Condens. Matter **16** R637.
- Watson, S. K., Potok, R. M., Marcus, C. M. and Umansky, V. (2003) Phys. Rev. Lett. **91** 258301
- Winkler, R. (2003) *Spin-Orbit Coupling Effects in Two-Dimensional Electron and Hole Systems*, Springer, Berlin.
- Wunderlich, J., Kaestner, B., Sinova, J. and Jungwirth, T. (2005) Phys. Rev. Lett. **94** 047204.
- Yoshida, S., Kanitani, Y., Oshima, R., Okada, Y., Takeuchi, O. and Shigekawa, H. (2007) Phys. Rev. Lett. **98** 026802.
- Zârbo, L. P. and Nikolić, B. K. (2007) EPL (Europhys. Lett.) **80** 47001.
- Zawadzki, W. (2005) Am. J. Phys. **73** 756.
- Žutić, I., Fabian, J. and Das Sarma, S. (2004) Rev. Mod. Phys. **76** 323.
- Zyuzin, V. A., Silvestrov, P. G. and Mishchenko, E. G. (2007) Phys. Rev. Lett. **99** 106601.